



Deposited via The University of Sheffield.

White Rose Research Online URL for this paper:

<https://eprints.whiterose.ac.uk/id/eprint/186588/>

Version: Accepted Version

Article:

Colombo, M. and Fairweather, M. (2019) Influence of multiphase turbulence modelling on interfacial momentum transfer in two-fluid Eulerian-Eulerian CFD models of bubbly flows. *Chemical Engineering Science*, 195. pp. 968-984. ISSN: 0009-2509

<https://doi.org/10.1016/j.ces.2018.10.043>

© 2018 Elsevier Ltd. This is an author produced version of a paper subsequently published in *Chemical Engineering Science*. Uploaded in accordance with the publisher's self-archiving policy. Article available under the terms of the CC-BY-NC-ND licence (<https://creativecommons.org/licenses/by-nc-nd/4.0/>).

Reuse

This article is distributed under the terms of the Creative Commons Attribution-NonCommercial-NoDerivs (CC BY-NC-ND) licence. This licence only allows you to download this work and share it with others as long as you credit the authors, but you can't change the article in any way or use it commercially. More information and the full terms of the licence here: <https://creativecommons.org/licenses/>

Takedown

If you consider content in White Rose Research Online to be in breach of UK law, please notify us by emailing eprints@whiterose.ac.uk including the URL of the record and the reason for the withdrawal request.

1 **Influence of multiphase turbulence modelling on interfacial momentum transfer in two-**
2 **fluid Eulerian-Eulerian CFD models of bubbly flows**

3
4 **Marco Colombo* and Michael Fairweather**

5 School of Chemical and Process Engineering, University of Leeds, Leeds LS2 9JT, UK

6 *Corresponding Author: M.Colombo@leeds.ac.uk; +44 (0) 113 343 2351

7
8 © 2019. This manuscript version is made available under the CC-BY-NC-ND 4.0 license
9 <http://creativecommons.org/licenses/by-nc-nd/4.0/>.

10 Published version <https://doi.org/10.1016/j.ces.2018.10.043>

11
12 **ABSTRACT**

13
14 Eulerian-Eulerian two-fluid computational fluid dynamic (CFD) models are increasingly used
15 to predict bubbly flows at an industrial scale. In these approaches, interface transfer is modelled
16 with closure models and correlations. Normally, the lateral void fraction distribution is
17 considered to mainly result from a balance between the lift and wall lubrication forces.
18 However, and despite the numerous models available that achieve, at least in pipe flows, a
19 reasonable predictive accuracy, agreement on a broadly applicable and accurate modelling
20 approach has not yet been reached. Additionally, the impact of turbulence modelling on the
21 lateral void fraction distribution has not, in general, been examined in detail. In this work, an
22 elliptic blending Reynolds stress model (EB-RSM), capable of resolving the turbulence field
23 in the near-wall region and improved to account for the contribution of bubble-induced
24 turbulence, is evaluated against best-practice $k-\varepsilon$ and high-Reynolds second-moment
25 turbulence closures. Lift and wall lubrication forces are initially deliberately neglected in the
26 EB-RSM. Comparisons for flows in pipes and a square duct show that the EB-RSM reproduces
27 the lateral void fraction distribution, including the peak in the void fraction in the near-wall
28 region, and reaches an accuracy comparable to the other two models noted above. In rod
29 bundles, even if none of the models considered performs with sufficient accuracy, the EB-RSM
30 detects features of the flow that are not predicted by the other two approaches. Overall, the
31 results demonstrate a much more prominent role of the turbulence structure and the induced
32 cross-sectional pressure field on the lateral void fraction distribution than is normally
33 considered. These effects need to be accounted for if more physically-consistent modelling of
34 bubbly flows is to be achieved. The lift force is added to the EB-RSM in the final part of the
35 paper, to provide a two-fluid formulation that can be used as the basis for additional
36 developments aimed at improving the accuracy and general applicability of two-fluid CFD
37 models.

38

39 **Keywords:** bubbly flow; two-fluid model; multiphase turbulence; Reynolds stress turbulence;
40 elliptic blending; void fraction distribution.

41

42 **1. Introduction**

43

44 Multiphase gas-liquid bubbly flows are frequently encountered in nature and are common in
45 industry and engineering applications, for example in heat exchangers, bubble column reactors,
46 nuclear reactors and in many oil and gas applications. Bubbles strongly affect the flow of the
47 continuous liquid phase and quantities such as the interfacial area concentration and the volume
48 fraction of the gas phase drive the design and operation of industrial equipment. Therefore,
49 research has been ongoing for many years to develop improved and more accurate models of
50 bubbly flows. Over the years, numerous experiments have been conducted. The continual
51 improvement of measurement techniques has made available progressively more detailed and
52 accurate experimental data. Serizawa et al. (1975) studied experimentally air-water upward
53 flows in a 60 mm inner diameter (ID) pipe at atmospheric pressure. Experiments in air-water
54 bubbly upward flows were also made by Liu and Bankoff (1993a, b) in a 38 mm ID pipe. In
55 both works, bubble velocity and diameter were measured with a two-sensor electrical resistivity
56 probe and liquid velocity and turbulence by hot-film anemometer probes. Talley et al. (2015)
57 measured bubble velocity, void fraction, interfacial area concentration and Sauter-mean
58 diameter in a 38.1 mm ID horizontal pipe using a four-sensor conductivity probe. Kim et al.
59 (2016) measured liquid and gas velocity and turbulent stresses in a 40 mm ID vertical pipe
60 using the two-phase particle image velocimetry technique. A few decades ago, mathematical
61 models were mainly limited to correlations or one-dimensional methods for predicting area-
62 averaged values of the interfacial area concentration or the void fraction (Ohkawa and Lahey,
63 1980; Coddington and Macian, 2002; Woldesemayat and Ghajar, 2007; Vasavada et al., 2009).
64 However, bubbly flows and multiphase gas-liquid flows in more general are multiscale in
65 nature, which constrains the modelling approaches above to mainly empirical treatments and
66 limited accuracy and applicability. To provide an example, coalescence of bubbles is governed
67 by trap, drainage and rupture of liquid films of micrometer thickness (Prince and Blanch, 1990;
68 Liao and Lucas, 2010). These microscale phenomena drive the formation of larger bubbles and
69 the evolution of the bubble diameter distribution strongly affects the average flow and the gas-
70 phase concentration at the component-scale level. The ability to handle such small-scale
71 phenomena in large, component-scale simulations has driven the recent development of
72 computational fluid dynamic (CFD) models, which has made possible the calculation of

73 detailed three-dimensional void fraction and interfacial area distribution fields (Yao and Morel,
74 2004; Nguyen et al., 2013; Rzehak and Krepper, 2013; Colombo and Fairweather, 2016).
75 Interface tracking techniques even allow prediction of the behaviour of individual bubbles in a
76 flow, though their applicability is still limited to a small number of bubbles due to run time
77 constraints. Dabiri and Tryggvason (2015) simulated a turbulent bubbly flow in a channel at
78 Reynolds numbers up to 5600 and with an imposed constant heat flux. 84 mono-dispersed
79 bubbles were tracked with a front tracking technique, with the void fraction kept constant at 3
80 % and with density ratio values up to 40. Feng and Bolotnov (2017) evaluated the bubble-
81 induced contribution to single-phase turbulence by resolving the interaction of a single bubble
82 and homogenous turbulence by using direct numerical simulation (DNS) and the level set
83 interface tracking method. Instead, for the prediction of industrial-scale flows, Eulerian-
84 Eulerian averaged two-fluid models have been the most frequent choice (Hosokawa and
85 Tomiyama, 2009; Colombo and Fairweather, 2015; Liao et al., 2015).

86

87 In Eulerian-Eulerian two-fluid models, the phases are treated as interpenetrating continua and
88 details of the interface structure are lost in the averaging procedure. Therefore, closure relations
89 are required to model interphase exchanges of mass, momentum and energy. In the majority of
90 studies, drag, lift, wall lubrication and turbulent dispersion forces have been considered to be
91 the dominant momentum coupling terms (Yao and Morel, 2004; Hosokawa and Tomiyama,
92 2009; Rzehak and Krepper, 2013; Colombo and Fairweather, 2015). In closed ducts, bubbles
93 have been repeatedly observed to obey two types of behaviour. Smaller spherical bubbles tend
94 to migrate towards the duct walls, generating a near-wall peak in the void fraction distribution.
95 Conversely, larger bubbles, whose shape is deformed by the inertia of the surrounding liquid,
96 move towards the centre of the duct. This effect can be attributed to a change in the direction
97 of the lift force, with the critical bubble diameter at which lift turns from positive to negative
98 being in the region of 4 to 6 mm (Tomiyama et al., 2002b; Lucas et al., 2010). As a result, in
99 most of the CFD studies performed to date, the lateral void fraction distribution is essentially
100 obtained from a balance between the lift and wall lubrication forces, with the additional effect
101 of turbulent dispersion working against void fraction gradients. Over the years, numerous lift
102 models have been developed, and many were optimized to predict the wall-peak void fraction
103 distribution observed in bubbly flow experiments in pipes (Serizawa et al., 1975; Liu and
104 Bankoff, 1993a, b). Even so, no general consensus has been reached on the most accurate
105 model, and an abundance of formulations exists (Hibiki and Ishii, 2007). This is because the
106 performance of the lift model is unavoidably related to the value of the other forces present,

107 and the wall lubrication force in particular. For the latter force, an even larger number of
108 slightly different prescriptions is available, with wall lubrication being totally neglected by
109 some authors. Antal et al. (1991) derived their wall force model from theoretical considerations
110 and assuming a spherical bubble shape and an irrotational flow. Yao and Morel (2004)
111 employed a constant lift coefficient equal to 0.5 and neglected any wall repulsive force.
112 Hosokawa and Tomiyama (2009) adopted the Tomiyama et al. (2002b) model for the lift force
113 and a model of the wall force they had developed a few years earlier (Hosokawa and
114 Tomiyama, 2003). Rzehak and Krepper (2013) modelled the lift force with the Tomiyama et
115 al. (2002b) model and for the wall force the Antal et al. (1991) model with coefficients modified
116 accordingly to the ANSYS CFX implementation. Colombo and Fairweather (2015) employed
117 a constant lift coefficient of 0.1 and the Antal et al. (1991) model with coefficients modified to
118 fit a large database of bubbly flows. Therefore, it is more accurate to say that an abundance of
119 coupled lift-wall lubrication force models exists.

120

121 In some recent works, a different and more complex structure of interfacial momentum transfer
122 has been identified and discussed. Ullrich et al. (2014) demonstrated the possibility of
123 predicting the near-wall peak of the void fraction profile even when neglecting the lift and wall
124 force contributions. In the authors' pipe flow simulations, the radial pressure gradient, induced
125 by the continuous phase turbulence field, was sufficient to induce the near-wall peak in the gas
126 phase void fraction. The authors employed a near-wall Reynolds stress model (RSM), able to
127 capture the anisotropy of the turbulence structure and the strong effect this has on the radial
128 distribution of the bubbles. This role of the continuous phase turbulence had been rarely
129 considered in previous works, in which multiphase extensions of single-phase linear eddy
130 viscosity models had generally been applied. To provide some examples, Troshko and Hassan
131 (2001), Yao and Morel (2004) and Sugrue et al. (2017) have adopted multiphase extensions of
132 the $k-\varepsilon$ model, while Rzehak and Krepper (2013) and Liao et al. (2015) employed the SST $k-\omega$
133 model. These works, in view of the intrinsic limitations of eddy viscosity-based turbulence
134 models, were unable to correctly predict the three-dimensional turbulence structure and its
135 influence on the void fraction distribution, in particular when, as is often done in single-phase
136 simulations, the turbulence kinetic energy is added to the pressure field. An exception was the
137 studies of Drew and Lahey (1982) and Lopez de Bertodano et al. (1990), which adopted a
138 Reynolds stress model of the turbulence to successfully predict the radial void fraction
139 distribution in circular pipes. Lahey et al. (1993) derived an algebraic RSM that predicted with
140 accuracy bubbly flows in triangular ducts. Recently, Mimouni et al. (2010, 2011) developed an

141 RSM for application in nuclear reactor thermal hydraulics. Comparison with bubbly flow
142 experiments in a 2×2 rod bundle show the improved accuracy of the RSM with respect to a
143 $k-\varepsilon$ model in these conditions. More recently, Santarelli and Frohlich (2015) simulated a
144 vertical bubbly flow in a channel using DNS and the immersed boundary method. A no-slip
145 boundary condition was applied at the interphase, representing air bubbles rising in water
146 contaminated with surfactants. From simulations of a fixed solid sphere in a shear flow, the
147 authors found that, even with spherical bubbles, the lift force can become negative with an
148 increase in the shear rate and the Reynolds number. This effect was attributed to the asymmetry
149 of the wake behind the sphere in a shear flow. Therefore, the wall-peaked profiles of the void
150 fraction distribution observed in bubbly flows were related to the action of the turbulence, and
151 more specifically to the turbophoresis effect. In a later paper, Santarelli and Frohlich (2016)
152 confirmed their findings with bubbles of different sizes. On increasing the bubble diameter, the
153 void fraction radial distribution was found to assume a core-peaked shape that the authors
154 attributed to a larger negative lift, high enough to overcome the action of turbophoresis.
155 Lubchenko et al. (2018), starting from experimental (Hassan, 2014) and DNS (Lu and
156 Tryggvason, 2013) evidence, questioned the physical basis of the wall lubrication force. Their
157 model predicts the wall-peaked void fraction distribution in pipe flows even without accounting
158 for wall lubrication, when a different formulation of the turbulent dispersion force is employed.
159

160 In this paper, modelling of the interphase momentum exchange in a two-fluid Eulerian-Eulerian
161 CFD model and the effect of the continuous phase turbulence field on the lateral void fraction
162 distribution of the dispersed phase are analysed. With respect to the previous works cited above
163 that employed high-Reynolds Reynolds-stress closures, a wall-resolved elliptic-blending
164 Reynolds stress model (EB-RSM) is adopted. The model is coupled to an interphase
165 momentum exchange closure where lift and wall lubrication forces are neglected and only
166 turbulent dispersion is considered in addition to the drag force. Results are compared to more
167 standard approaches based on high-Reynolds number $k-\varepsilon$ and Reynolds stress turbulence
168 models that include lift and wall force contributions. The models are tested not only in pipes,
169 but also in a square duct and in a rod bundle. Compared to pipes, square ducts and rod bundles
170 have received less attention in the literature, and the accuracy of lift and wall force models in
171 these geometries is much less well established. A selection of experiments characterized by a
172 mono-dispersed bubble size distribution allows the analysis to focus on turbulence and
173 interphase closure modelling. The role of the different interphase forces in a two-fluid model,
174 and of the lift-wall lubrication balance on the lateral void fraction distribution, are discussed.

175 More specifically, the action of the turbulence structure on the void fraction distribution and
176 the benefits of high order turbulence modelling for overall two-fluid model accuracy and
177 generality are addressed. Finally, the addition of the lift force to the EB-based two-fluid model
178 is evaluated as a basis for further developments in the CFD modelling of bubbly flows.

179

180 **2. Experimental data**

181

182 Numerical results are compared against air-water bubbly flow experimental data obtained in
183 three geometries, namely a pipe, a square duct and a rod bundle. More specifically, two pipe
184 flows are taken from Liu and Bankoff (1993a) and Hosokawa and Tomiyama (2009), the square
185 duct flow from Sun et al. (2014) and the rod bundle flow from Hosokawa et al. (2014).

186

187 Liu and Bankoff (1993a, b) investigated upward air-water bubbly flows inside a vertical pipe
188 of 38 mm inside diameter. Liquid mean velocities and turbulent fluctuations were measured
189 using one and two-dimensional hot-film anemometer probes, and bubble velocity, void fraction
190 and frequency with an electrical resistivity probe. Measurements were taken for 48 flow
191 conditions that covered the ranges $0.376\text{-}1.391\text{ m s}^{-1}$ for the liquid superficial velocity, 0.027-
192 0.347 m s^{-1} for the air superficial velocity and $0.0\text{-}0.5$ for the void fraction.

193

194 Hosokawa and Tomiyama (2009) studied air-water bubbly flows flowing upward in a vertical
195 pipe having an inside diameter of 25 mm. Liquid velocities were measured with using laser
196 Doppler velocimetry and two high-speed cameras were used to obtain stereoscopic images of
197 the bubbles. From these images, the authors reconstructed the bubble number, size and shape,
198 and the bubble velocity. Measurements were obtained in the ranges $0.5\text{-}1.0\text{ m s}^{-1}$ for the liquid
199 superficial velocity, $0.018\text{-}0.036\text{ m s}^{-1}$ for the air superficial velocity, $0.0146\text{-}0.0399$ for the
200 void fraction and $3.21\text{-}4.25\text{ mm}$ for the bubble diameter.

201

202 Sun et al. (2014) measured upward air-water bubbly flows in a vertical square duct having a
203 side length of 0.136 m . X-type hot-film anemometry was used to measure the velocity of the
204 liquid phase and a multi-sensor optical probe and a high-speed camera for measurements in the
205 gas phase. Local values of the void fraction, the bubble diameter and frequency, the mean water
206 velocity and the turbulence kinetic energy were measured for 11 two-phase flow conditions.
207 Measurements were taken along parallel lines in the two directions perpendicular to the duct
208 axis using a resolution of 121 measurement points in each quarter square area of the cross-

209 section. Measurements covered the ranges 0.5-1.0 m s⁻¹ for the liquid superficial velocity, 0.045
210 -0.226 m s⁻¹ for the air superficial velocity and 0.069-0.172 for the void fraction.

211

212 Hosokawa et al. (2014) experimentally studied upward air-water bubbly flow in a vertical 4×4
213 rod bundle. The outer diameter of the rods was 10 mm and the pitch 12.5 mm. The rod bundle
214 was contained inside a square box having a side length of 54 mm and a corner radius of 8.25
215 mm. The void fraction distribution and bubble velocity in various sub-channels were measured
216 by a double-sensor conductivity probe. Liquid velocity was measured using a laser Doppler
217 velocimetry technique. Measurements covered the ranges 0.9-1.5 m s⁻¹ for the liquid superficial
218 velocity, 0.06-0.15 m s⁻¹ for the air superficial velocity and 0.0-0.22 for the void fraction.

219

220 Initially, results are compared with a pipe flow experiment from Hosokawa and Tomiyama
221 (2009). To extend the comparison to higher void fractions, a pipe flow from Liu and Bankoff
222 (1993a) is subsequently considered. Finally, comparison is made with a flow from the square
223 duct database of Sun et al. (2014) and a flow from the rod bundle database of Hosokawa et al.
224 (2014). Using the information available on the bubble diameter, specific experiments were
225 selected to have bubbles characterized by a homogeneous mono-dispersed size distribution.
226 Bubbles maintain a spherical or slightly deformed shape. Consequently, all the bubbles show
227 a similar behaviour and the population can be effectively characterized by the average diameter
228 of the mono-dispersed distribution (Besagni et al., 2018). This is confirmed by the measured
229 bubble diameter distribution, when available (Liu and Bankoff, 1993b; Hosokawa and
230 Tomiyama, 2009), and by the wall-peaked void profiles recorded in all four experiments.
231 Experimental conditions are summarized in Table 1 and details on the selection of the average
232 bubble diameter in the CFD simulations are provided later in Section 4.

233

234

235

Table 1. Summary of experiments used to assess CFD simulations.

Experiment	j_w [m s⁻¹]	j_a [m s⁻¹]	Geometry	D_h [m]
Hosokawa and Tomiyama (2009)	1.0	0.036	Pipe	0.025
Liu and Bankoff (1993a)	0.753	0.180	Pipe	0.038
Sun et al. (2014)	0.75	0.09	Square duct	0.136
Hosokawa et al. (2014)	0.9	0.06	4 × 4 Rod bundle	0.009

236

237 3. CFD model

238

239 In the two-fluid Eulerian-Eulerian approach, each phase is described by a set of averaged
240 conservation equations. Adiabatic air-water flows are considered in this work, therefore only

241 the continuity and momentum equations are necessary, with the phases treated as
 242 incompressible with constant properties:

243

$$\frac{\partial}{\partial t}(\alpha_k \rho_k) + \frac{\partial}{\partial x_i}(\alpha_k \rho_k U_{i,k}) = 0 \quad (1)$$

244

$$\begin{aligned} \frac{\partial}{\partial t}(\alpha_k \rho_k U_{i,k}) + \frac{\partial}{\partial x_j}(\alpha_k \rho_k U_{i,k} U_{j,k}) \\ = -\alpha_k \frac{\partial}{\partial x_i} p_k + \frac{\partial}{\partial x_j} [\alpha_k (\tau_{ij,k} + \tau_{ij,k}^{Re})] + \alpha_k \rho_k g_i + M_{i,k} \end{aligned} \quad (2)$$

245

246 In the above equations, α_k represents the volume fraction of phase k , whereas in the following
 247 α is used to specify the void fraction of air. ρ is the density, U the velocity, p the pressure and
 248 g the gravitational acceleration. τ and τ^{Re} are the laminar and turbulent stress tensors,
 249 respectively, and M_k is the interfacial momentum transfer source. When using the EB-RSM,
 250 only the drag force and turbulent dispersion force are considered, and the lift and the wall
 251 lubrication forces are neglected. In contrast, when the high Reynolds number k - ϵ model and
 252 RSM are used, the lift and wall contributions are included.

253

254 **3.1. Interfacial momentum transfer**

255

256 The drag force is an expression of the resistance opposed to bubble motion relative to the
 257 surrounding liquid. The model of Tomiyama et al. (2002a), which accounts for the effect of the
 258 bubble aspect ratio, is used to predict the drag coefficient C_D :

259

$$C_D = \frac{8}{3} \frac{Eo}{E^{2/3}(1 - E^2)^{-1}Eo + 16E^{4/3}} F^{-2} \quad (3)$$

260

261 The drag coefficient is a function of the Eötvös number ($Eo = \Delta\rho g d_B / \sigma$, where σ is the surface
 262 tension) and bubble aspect ratio E . F in Eq. (3) is an additional function of the bubble aspect
 263 ratio. The bubble aspect ratio is calculated from a correlation and it is function of the distance
 264 from the wall y_w :

265

$$E = \max \left[1.0 - 0.35 \frac{y_w}{d_B}, E_0 \right] \quad (4)$$

266

267 Eq. (4) follows experimental evidence that shows that the aspect ratio increases and tends to a
 268 value of 1 (perfectly spherical bubble) as the wall is approached. As a consequence, the drag
 269 coefficient increases and a reduction in the relative velocity between the bubbles and the fluid

270 is observed in the near-wall region (Hosokawa and Tomiyama, 2009). The reference value E_0
 271 is obtained from the correlation of Welleck et al. (1966). An additional correction is also
 272 included to account for drag reduction due to bubble swarm (Tomiyama et al., 1998):

$$273 \quad C_D = C_{D,0} \alpha^{-0.5} \quad (5)$$

274 Each bubble moving in a shear flow experiences a lift force perpendicular to its direction of
 275 motion. Therefore, the lift force influences the lateral movement of the bubbles and the void
 276 fraction distribution. Generally, a positive value of the lift coefficient characterizes spherical
 277 bubbles, which are therefore pushed towards the wall. Larger bubbles that are deformed by
 278 inertial forces experience a change of sign in the lift force and are pushed towards the centre
 279 of the flow (Ervin and Tryggvason, 1997; Tomiyama et al., 2002b). Over the years, numerous
 280 models have been proposed. Amongst others, the correlation from Tomiyama et al. (2002b) is
 281 frequently used (Rzehak and Krepper, 2013; Liao et al., 2015):

$$283 \quad C_L = \begin{cases} \min[0.288 \tanh(0.121 Re_b), f(Eo_d)] & Eo_d < 4 \\ f(Eo_d) & 4 < Eo_d < 10 \\ -0.27 & Eo_d > 10 \end{cases} \quad (6)$$

284 In Eq. (6), Re_B is the bubble Reynolds number ($Re_B = \rho_c U_r d_B / \mu_c$, where the density and
 285 viscosity of the continuous phase c are used, and U_r is the magnitude of the relative velocity).
 286 Eo_d is a modified Eötvös number where the maximum horizontal dimension of the bubble,
 287 obtained using the aspect ratio from Welleck et al. (1966), is employed. $f(Eo_d)$ is a function of
 288 the modified Eötvös number:

$$290 \quad f(Eo_d) = 0.00105 Eo_d^3 - 0.0159 Eo_d^2 - 0.0204 Eo_d + 0.474 \quad (7)$$

291 In this work, results are compared against data using a constant value of the lift coefficient C_L
 292 = 0.1, adopted by other researchers who reported good agreement with experimental
 293 measurements (Lopez de Bertodano et al., 1994; Lahey and Drew, 2001; Colombo and
 294 Fairweather, 2015). In the past, agreement with data has been reported for values of the lift
 295 coefficient ranging from 0.01 (Wang et al., 1987; Yeoh and Tu, 2006) to 0.5 (Mimouni et al.,
 296 2010), and it is therefore difficult to make further comments on the accuracy of different lift
 297 force models. Clearly, however, the use of constant lift coefficient forces the choice to be made
 298 between a wall- or a core-peaked void fraction profile before any simulation. However, the
 299 present study is limited to flows exhibiting wall-peaked void fraction profiles.

301

302 A bubble depleted region characterizes the portion of a flow very close to the wall. Normally,
 303 this has been modelled using the influence of the wall lubrication force, generated by the
 304 asymmetric flow distribution around the bubbles flowing close to a solid wall (Antal et al.,
 305 1991):

$$\mathbf{F}_w = \max\left(0, C_{w,1} + C_{w,2} \frac{d_B}{y_w}\right) \alpha \rho_c \frac{|\mathbf{U}_r|^2}{d_B} \mathbf{n}_w \quad (8)$$

306 In the previous equation, \mathbf{n}_w is the normal to the wall, and C_{w1} and C_{w2} modulate the strength
 307 and the region of influence of the wall force. If numerous values and models of the lift
 308 coefficient can be found in literature, even more have been proposed for C_{w1} and C_{w2} . Often,
 309 their values depend on the experimental data set being predicted and the lift force model used
 310 and, consequently, a lot of uncertainty exists. In this work, values are taken from Colombo
 311 and Fairweather (2015), where numerous bubbly flows in pipes were predicted using $C_{w1} = -$
 312 0.4 and $C_{w2} = 0.3$ with a k - ε turbulence model, and $C_{w1} = -0.65$ and $C_{w2} = 0.45$ with a Reynolds
 313 stress turbulence model.
 314

315 The turbulent dispersion force is modelled after Burns et al. (2004) who derived an expression
 316 by applying Favre-averaging to the drag force:
 317

$$\mathbf{F}_{td} = \frac{3}{4} \frac{C_D \alpha \rho_c |\mathbf{U}_r|}{d_B} \frac{\nu_{t,c}}{\sigma_\alpha} \left(\frac{1}{\alpha} + \frac{1}{(1-\alpha)} \right) \nabla \alpha \quad (9)$$

318 Here, $\nu_{t,c}$ is the turbulent kinematic viscosity of the continuous phase and σ_α the turbulent
 319 Prandtl number for the volume fraction, assumed equal to 1.0.
 320

322 **3.2. Multiphase turbulence modelling**

323 Turbulence is resolved in the continuous phase using Reynolds-averaged Navier-Stokes
 324 (RANS) turbulence models. Three models are used: a high-Reynolds number k - ε model and
 325 RSM, and the EB-RSM that allows solution of the flow field up to the near-wall region.
 326

327 The k - ε model uses a multiphase formulation of the standard model from Jones and Launder
 328 (1972), and balance equations for the turbulence kinetic energy k and the turbulence energy
 329 dissipation rate ε are given as (CD-adapco, 2016):
 330

331

$$\begin{aligned}
& \frac{\partial}{\partial t}((1-\alpha)\rho_c k_c) + \frac{\partial}{\partial x_i}((1-\alpha)\rho_c U_{i,c} k_c) \\
& = \frac{\partial}{\partial x_i} \left[(1-\alpha) \left(\mu_c + \frac{\mu_{t,c}}{\sigma_k} \right) \frac{\partial k_c}{\partial x_i} \right] + (1-\alpha)(P_{k,c} - \rho_c \varepsilon_c) \\
& + (1-\alpha)S_k^{BI}
\end{aligned} \tag{10}$$

333

$$\begin{aligned}
& \frac{\partial}{\partial t}((1-\alpha)\rho_c \varepsilon_c) + \frac{\partial}{\partial x_i}((1-\alpha)\rho_c U_{i,c} \varepsilon_c) \\
& = \frac{\partial}{\partial x_i} \left[(1-\alpha) \left(\mu_c + \frac{\mu_{t,c}}{\sigma_\varepsilon} \right) \frac{\partial \varepsilon_c}{\partial x_i} \right] + (1-\alpha) \frac{\varepsilon_c}{k_c} (C_{\varepsilon,1} P_{k,c} - C_{\varepsilon,2} \rho_c \varepsilon_c) \\
& + (1-\alpha)S_\varepsilon^{BI}
\end{aligned} \tag{11}$$

334

335 In Eqs. (10) and (11), $P_{k,c}$ is the production term due to shear and S_k^{BI} and S_ε^{BI} the source terms
336 due to bubble-induced turbulence. The turbulent viscosity $\mu_{t,c}$ is evaluated from the single-
337 phase k - ε formulation:

338

$$\mu_{t,c} = C_\mu \rho_c \frac{k_c^2}{\varepsilon_c} \tag{12}$$

339

340 Turbulence in the dispersed phase is not explicitly resolved, but it is obtained from the
341 continuous phase turbulence field:

342

$$\mu_{t,d} = \frac{\rho_d}{\rho_c} C_t^2 \mu_{t,c} \tag{13}$$

343

344 with C_t assumed equal to 1. This approximation, valid for dispersed two-phase flow, is justified
345 in view of the very low value of the density ratio in air-water flows, which causes the Reynolds
346 stress in the gas to be much smaller than in the liquid (Gosman et al., 1992; Behzadi et al.,
347 2004).

348 The bubble contribution to the turbulence is accounted for by considering the conversion of
349 energy lost by the bubbles to drag into turbulence kinetic energy in the bubble wakes (Kataoka
350 and Serizawa, 1989; Troshko and Hassan, 2001; Rzehak and Krepper, 2013). The turbulence
351 kinetic energy equation source term S_k^{BI} is expressed as:

352

$$S_k^{BI} = K_{BI} \mathbf{F}_d \mathbf{U}_r \tag{14}$$

353

354 \mathbf{F}_d is the drag force and K_{BI} is introduced to account for the modulation of the turbulence source.

355 In the turbulence energy dissipation rate equation, the bubble-induced source is expressed as
356 the corresponding turbulence kinetic energy source term, but multiplied by the timescale of the
357 bubble-induced turbulence τ_{BI} :

358

$$S_{\varepsilon}^{BI} = \frac{C_{\varepsilon, BI}}{\tau_{BI}} S_k^{BI} \quad (15)$$

359

360 In shear-induced single-phase turbulence modelling, the turbulence timescale corresponds to
 361 the lifetime of a turbulent eddy before it breaks up into smaller structures. In multiphase
 362 turbulence, the situation is more complex and the bubble-induced turbulence timescale should
 363 also be related to the bubble length and velocity scales. At the present time, a generally accepted
 364 formulation is yet to emerge. In this work, the recent proposal of a mixed timescale from
 365 Rzehak and Krepper (2013) is adopted. Consequently, the velocity scale is derived from the
 366 square root of the liquid turbulence kinetic energy and the length scale from the bubble
 367 diameter. In addition, a value of $K_{BI} = 0.25$ is used in Eq. (14), this value having been arrived
 368 at through optimization by Colombo and Fairweather (2015) when predicting a large database
 369 of bubbly flows.

370

371 The multiphase Reynolds stress turbulence model formulation adopted is based on the single-
 372 phase transport equations of the Reynolds stresses, $R_{ij} = \tau_{i,j}^{Re} / \rho_c$ (CD-adapco, 2016):

373

$$\begin{aligned} \frac{\partial}{\partial t} \left((1 - \alpha) \rho_c R_{ij} \right) + \frac{\partial}{\partial x_j} \left((1 - \alpha) \rho_c U_{i,c} R_{ij} \right) \\ = \frac{\partial}{\partial x_j} \left[(1 - \alpha) D_{R,ij} \right] + (1 - \alpha) (P_{ij} + \rho_c \Phi_{ij} - \rho_c \varepsilon_{ij}) + (1 - \alpha) S_{ij}^{BI} \end{aligned} \quad (16)$$

374

375 Here, P_{ij} is the turbulence production. The Reynolds stress diffusion $D_{R,ij}$ is modelled
 376 accordingly to Daly and Harlow (1970), whilst the isotropic hypothesis is used for the
 377 turbulence dissipation rate term ε_{ij} . Φ_{ij} is the pressure-strain model accounting for pressure
 378 fluctuations that redistribute the turbulence energy amongst the various Reynolds stress
 379 components. The pressure-strain relation is modelled using the so-called ‘‘SSG model’’
 380 (Speziale et al., 1991), which is quadratically non-linear in the turbulence anisotropy tensor:

381

$$\begin{aligned} \Phi_{ij}^h = -[C_{1a}\varepsilon + C_{1b}tr(P)]a_{ij} + C_2\varepsilon \left(a_{ik}a_{kj} - \frac{1}{3}a_{mn}a_{mn}\delta_{ij} \right) \\ + \left[C_{3a} - C_{3b}(a_{ij}a_{ij})^{0.5} \right] kS_{ij} \\ + C_4k \left(a_{ik}S_{jk} + a_{jk}S_{ik} - \frac{2}{3}a_{mn}S_{mn}\delta_{ij} \right) + C_5(a_{ik}W_{jk} + a_{jk}W_{ik}) \end{aligned} \quad (17)$$

382

383 Here, a_{ij} are components of the anisotropy tensor, and S_{ij} and W_{ij} are the strain rate and the
 384 rotation rate tensors, respectively. The bubble-induced turbulence source term is calculated
 385 using Eq. (14). The source is then split amongst the normal Reynolds stress components

386 according to Colombo and Fairweather (2015), who apportion a higher fraction of the bubble-
 387 induced turbulence source to the streamwise direction (Lopez de Bertodano et al., 1990):

388

$$S_{ij}^{BI} = \begin{bmatrix} 1.0 & 0.0 & 0.0 \\ 0.0 & 0.5 & 0.0 \\ 0.0 & 0.0 & 0.5 \end{bmatrix} S_k^{BI} \quad (18)$$

389

390 A high Reynolds number wall treatment, where the velocity in the first near-wall computational
 391 cell is imposed from the single-phase law of the wall, is used with both the k - ε model and the
 392 RSM. The EB-RSM (Manceau and Hanjalic, 2002; Manceau, 2015), in contrast, blends the
 393 quasi-homogeneous SSG model from Eqs. (16) and (17) with a near-wall formulation that
 394 reproduces the correct asymptotic behaviour of the turbulent stresses near the wall. In the
 395 vicinity of a wall the turbulence field is strongly anisotropic and the impermeability
 396 requirement at the wall exerts a kinematic blockage effect on the wall-normal velocity
 397 fluctuations. At the same time, the wall reflects pressure fluctuations, the so-called wall echo
 398 effect, which, in opposition to wall blockage, favours the redistribution of energy to the wall-
 399 normal component of the turbulence. The correct asymptotic behaviour of the pressure-strain
 400 relation near a wall is modelled using the following relation:

401

$$\Phi_{ij}^w = -5 \frac{\varepsilon}{k} \left[\overline{u_l u_k} n_j n_k + \overline{u_j u_k} n_i n_k - \frac{1}{2} \overline{u_k u_l} n_k n_l (n_i n_j + \delta_{ij}) \right] \quad (19)$$

402

403 In the previous equation, n are the components of the wall-normal vector. Transition from the
 404 near-wall model in Eq. (19) to the weakly inhomogeneous behaviour away from the wall is
 405 ensured by the elliptic relaxation function α_{EB} :

406

$$\Phi_{ij} = (1 - \alpha_{EB}^3) \Phi_{ij}^w + \alpha_{EB}^3 \Phi_{ij}^h \quad (20)$$

407

408 The elliptic relaxation function is obtained by solving the following elliptic relaxation equation
 409 with the $\alpha_{EB} = 0$ wall boundary condition:

410

$$\alpha_{EB} - L_t \nabla^2 \alpha_{EB} = 1 \quad (21)$$

411

412 The turbulent length scale L_t then follows from:

413

$$L_t = C_l \max \left(C_\eta \frac{v^{3/4}}{\varepsilon^{1/4}}, \frac{k^{3/2}}{\varepsilon} \right) \quad (22)$$

414

415 Similarly, the near-wall behaviour of the turbulence energy dissipation rate is imposed using
 416 the elliptic relaxation function:

417

$$\varepsilon_{ij} = (1 - \alpha_{EB}^3) \frac{\overline{u_i u_j}}{k} \varepsilon + \frac{2}{3} \alpha_{EB}^3 \varepsilon \delta_{ij} \quad (23)$$

418

419 At the wall, the following boundary condition is used for the turbulence energy dissipation rate:

420

$$\varepsilon = 2\nu \lim_{y_w \rightarrow 0} \frac{k}{y_w^2} \quad (24)$$

421

422 Values of all the model coefficients used can be found in Table 2. The model for the bubble-

423 induced contribution to the continuous phase turbulence (Eqs. (14) and (15)) has been

424 implemented in the EB-RSM, this being vital to obtaining accurate predictions of the

425 turbulence intensity in bubbly flows (Colombo and Fairweather, 2015). The bubble-induced

426 contribution is partitioned among the normal turbulent stress components using Eq. (18).

427 A summary of the turbulence and interfacial closures used in the different models is provided

428 in Table 3, together with the experiments predicted with each model.

429

430

Table 2. Coefficients used in the various turbulence models.

431

C_μ	$C_{\varepsilon,1}$	$C_{\varepsilon,2}$	σ_k	σ_ε	K_{BI}	$C_{\varepsilon,BI}$	C_{Ia}
0.09	1.44	1.92	1.0	1.3	0.25	1.0	1.7
C_{Ib}	C_2	C_{3a}	C_{3b}	C_4	C_5	C_l	C_η
0.9	1.05	0.8	0.65	0.625	0.2	0.133	80

432

433

Table 3. Summary of the model settings and experiments predicted.

	EB-RSM	RSM	$k - \varepsilon$	$k - \varepsilon$ Tomiyama
Turbulence	SSG RSM (Speziale et al., 1991). Elliptic Blending near-wall treatment	SSG RSM (Speziale et al. 1991). High-Reynolds number wall treatment	$k - \varepsilon$ (Jones and Launder, 1972). High-Reynolds number wall treatment	$k - \varepsilon$ (Jones and Launder, 1972). High-Reynolds number wall treatment
Bubble-induced turbulence	Colombo and Fairweather (2015)	Colombo and Fairweather (2015)	Colombo and Fairweather (2015)	Colombo and Fairweather (2015)
Drag	Tomiyama et al. (2002a)	Tomiyama et al. (2002a)	Tomiyama et al. (2002a)	Tomiyama et al. (2002a)
Lift	Neglected	Constant coefficient. $C_L = 0.1$	Constant coefficient. $C_L = 0.1$	Tomiyama et al. (2002b)
Wall Lubrication	Neglected	Antal et al. (1991). $C_{w1} = -0.4$ $C_{w2} = 0.3$	Antal et al. (1991). $C_{w1} = -0.65$ $C_{w2} = 0.45$	Antal et al. (1991). $C_{w1} = -0.4$ $C_{w2} = 0.3$
Turbulent Dispersion	Burns et al. (2004)	Burns et al. (2004)	Burns et al. (2004)	Burns et al. (2004)
Experiments*	HT, LB, Sun, Hos	HT, LB, Sun, Hos	HT, LB, Sun, Hos	HT, LB

435 *In relation to Table 1: HT: Hosokawa and Tomiyama (2009); LB: Liu and Bankoff (1993a); Sun: Sun et al. (2014); Hosokawa
436 et al. (2014).

437

438 3.3. Numerical settings

439 Numerical simulations were performed using the STARCCM+ code (CD-adapco, 2016). Pipe
440 flows were simulated in a two-dimensional axisymmetric geometry, whereas 1/4 sections were
441 used for both the square duct and the rod bundles. Constant inlet phase velocity and void
442 fraction boundary conditions were imposed. Pressure was fixed on the outlet section. Flow
443 conditions were fully-developed and a zero gradient condition was imposed on all other flow
444 quantities. The no-slip boundary condition was imposed at the wall. For the high-Reynolds
445 number wall treatment, velocity in the near-wall cell was imposed from the single-phase law
446 of the wall. For the EB-RSM model, the velocity field was finely resolved in the near-wall
447 region. Turbulence in this region was handled by modelling the asymptotic behaviour of the
448 pressure-strain relation and the turbulence dissipation rate using the elliptic blending approach
449 (Section 3.2). At the wall, zero values of the turbulent stresses were imposed. For the turbulence
450 dissipation rate, the limit $\varepsilon = 2\nu(k/y_w)_{y_w \rightarrow 0}$ was imposed.

451 Uniform profiles of water and vapour velocity, and the void fraction, were obtained from
452 superficial velocities (Table 1) from the experiments and imposed at the inlet section. A small
453 amount of turbulence (intensity $\sim 1\%$) was also imposed. The same values of velocity, void

454 fraction and turbulence intensity were used for the initial condition. Results were recorded at a
455 sufficient distance from the inlet to ensure the flow had reached fully-developed conditions and
456 any influence of the inlet conditions had disappeared. Detailed measurements of the bubble
457 diameter distribution at different heights after bubble injection are a rarity in the literature and
458 no measurements of this kind are available for the experiments considered. However,
459 experiments were selected from mono-dispersed bubble size distribution tests that can be
460 characterized reasonably-well with a single average bubble diameter. In addition the bubble
461 diameter in the simulations was fixed using averaged values or local lateral profiles that were
462 available at the measurement plane for all 4 experiments. This, in conjunction with the mono-
463 dispersed size distribution, ensured that simulations were representative of local experimental
464 conditions at the measurement plane, even without accounting for break up and coalescence
465 through, for example, a population balance equation. Specifically, the bubble diameter was set
466 to $d_B = 3.66$ mm for Hosokawa and Tomiyama (2009) and $d_B = 3.0$ mm for Liu and Bankoff
467 (1993a), based on the bubble diameter distributions available. Values for Sun et al. (2014) and
468 Hosokawa et al. (2014) were obtained from averaging the lateral profile at the measurement
469 plane. These profiles show an almost constant average bubble diameter across the cross-
470 section, with values $d_B = 4.25$ mm for Sun et al. (2014) and $d_B = 3.0$ mm for Hosokawa et al.
471 (2014). For Sun et al. (2014) the value is slightly higher and approaches the transition region
472 where the behaviour of the bubbles (and the direction of the lift force) change, driven by the
473 deformation of their shape. However, wall-peaked void fraction profiles from the experiment
474 reasonably suggest that the bubbles still preferentially accumulate towards the wall and the
475 mono-dispersed approximation (and a positive lift coefficient) still holds. Using CFD results,
476 values of the bubble Reynolds, Eötvös and Morton numbers have been calculated and are
477 reported in Table 4. The Reynolds number range is representative of bubbles in the wall region
478 (low value) and in the centre of the duct (high value). According to the classification of Clift
479 et al. (1978), the bubble shape is on the boundary between spherical (at the wall) and slightly
480 deformed-ellipsoidal bubbles (in the centre). Even in the centre, however, deformation does
481 not approach the cap-bubble shape that determines the change of bubble behaviour
482 (accumulation in the centre driven by the lift force).

483 Table 4. Bubble characteristics in the four experiments

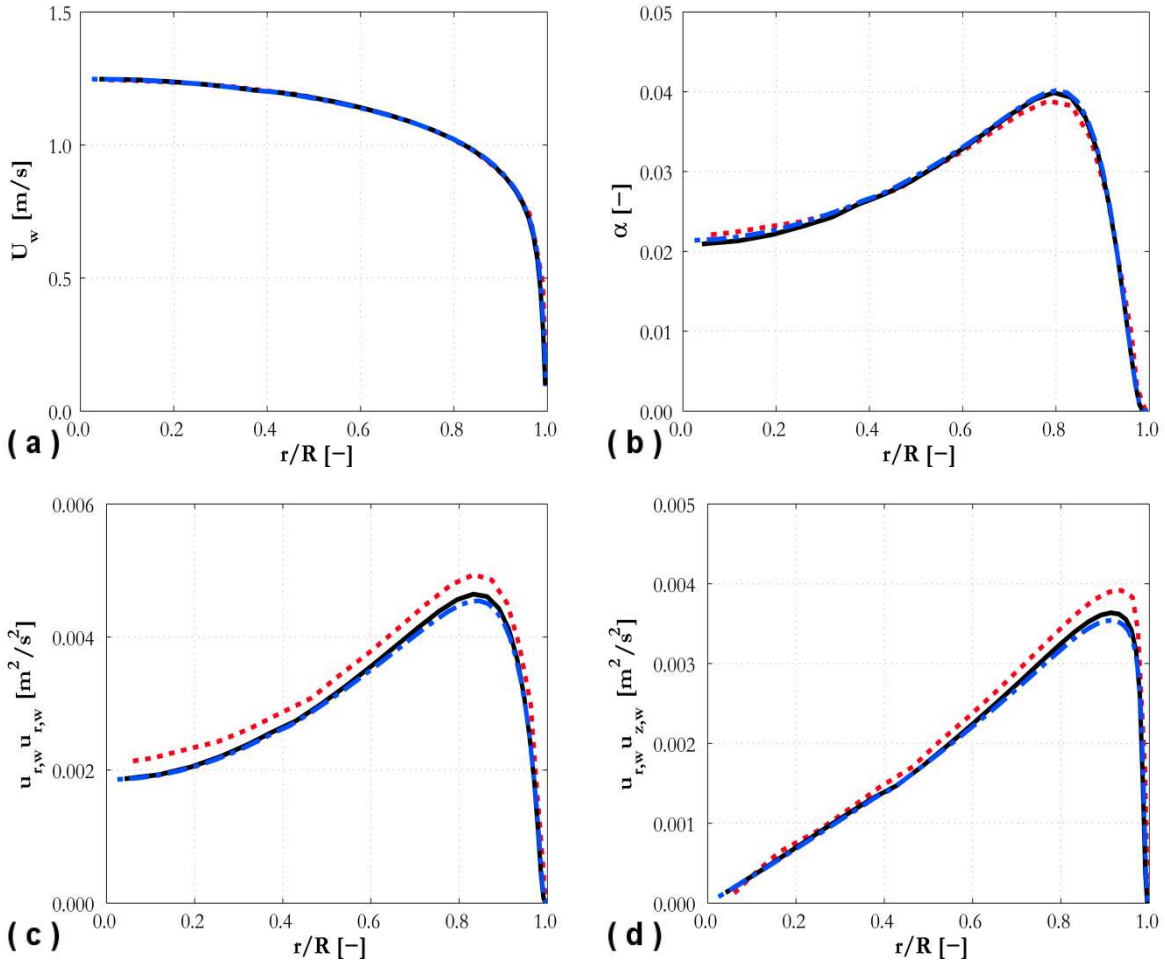
Experiment	d_B [m]	Re_B [-]	Eo [-]	Mo [-]
Hosokawa and Tomiyama (2009)	0.00366	300-675	1.8	$1.36 \cdot 10^{-13}$
Liu and Bankoff (1993a)	0.003	130-640	1.21	$1.36 \cdot 10^{-13}$
Sun et al. (2014)	0.00425	545-1120	2.42	$3.623 \cdot 10^{-14}$
Hosokawa et al. (2014)	0.003	330-650	1.21	$8.48 \cdot 10^{-14}$

484

485 Pressure-velocity coupling was solved using a multiphase extension of the SIMPLE algorithm
486 and second-order upwind schemes were used to discretize the velocity, volume fraction,
487 turbulent stresses, turbulence kinetic energy and dissipation rate convective terms. Under-
488 relaxation factors of 0.5 for the momentum equations, 0.4 for the pressure, 0.25 for the void
489 fraction and 0.6 for the turbulence were found sufficient to ensure a smooth convergence of
490 the results. Simulations were advanced in time with a second-order implicit scheme. The
491 Courant number was kept under a maximum value of 2 and, after an inlet development region,
492 fully developed steady-state conditions were reached before recording the results. Strict
493 convergence of residuals (pressure, velocity, volume fraction and turbulence quantities) was
494 ensured ($< 10^{-5}$) and the mass balance was checked to have an error always less than 0.1 % for
495 both phases.

496
497 Structured meshes were employed and sensitivity studies were made to ensure mesh-
498 independent solutions. For the high Reynolds number turbulence models, care was taken to
499 ensure the first near-wall grid point was always located at a non-dimensional distance from the
500 wall y^+ greater than 30, in the region of validity of the law of the wall. In contrast, the EB-RSM
501 model requires a much more refined mesh in the near-wall region. In this region, solutions of
502 the transport equations away from the wall are blended with a near-wall model for the
503 turbulence stresses and the turbulence energy dissipation rate. Results of the mesh sensitivity
504 study are reported in detail for the Hosokawa and Tomiyama (2009) pipe flow experiment.
505 Three different meshes were tested, with the number of elements equal to 20×500 , 26×800
506 and 40×1500 . Radial profiles of the water mean velocity, void fraction, radial turbulent stress
507 and Reynolds shear stress are provided in Figure 1. The void fraction and velocity profiles do
508 not show any meaningful differences between the three meshes considered. For the turbulence
509 parameters, the solution changes from the least-refined to the medium grid, with additional
510 refinement then showing no significant changes in the radial profiles given in Figure 1.
511 Consequently, the medium mesh (20,800 cells) was selected for the simulations employing the
512 EB-RSM. Similar studies were made for the Liu and Bankoff (1993a), Sun et al. (2014) and
513 Hosokawa et al. (2014) experiments, and mesh-independent solutions were obtained using
514 44,800 (in two-dimensional axisymmetry), 1,280,000 and 369,600 cells, respectively. In all the
515 meshes, the centre of the near-wall cell was located at a wall distance y^+ in the range 1 – 1.5,
516 sufficient for the application of the elliptic blending modelling strategy. Corresponding meshes
517 for the high Reynolds models employed 3,750, 129,375 and 146,825 cells, with 3000 used for
518 the experiment of Hosokawa and Tomiyama (2009).

519



520

521

522

523

524

525

526

527

528

529

530

531

532

533

534

535

536

537

Figure 1. Mesh sensitivity study for the Hosokawa and Tomiyama (2009) experiment: (a) water mean velocity; (b) air void fraction; (c) radial turbulent stress; and (d) Reynolds shear stress (--- 175×500 ; — 276×800 ; - - - 700×1500).

4. Results and discussion

4.1. Pipe flows

The Hosokawa and Tomiyama (2009) experiment was simulated first with the EB-RSM and the predicted void fraction profile is shown in Figure 2. Interestingly, the wall-peaked void profile that characterizes bubbly flows in pipes is clearly visible, even if the lift force and wall lubrication are neglected. Although, the value of the peak is underestimated and too high values of the void fraction are predicted in the centre of the pipe. At steady-state, and in the absence of lift and wall forces, in a pipe the momentum balance in the radial direction for the liquid and the gas phase reduces to:

$$\frac{\alpha_l \partial p}{\rho_l \partial r} = \frac{F_{td,r}}{\rho_l} - \frac{\partial \alpha_l \overline{u_r u_r}^l}{\partial r} + \frac{\alpha_l}{r} (\overline{u_\theta u_\theta}^l - \overline{u_r u_r}^l) \quad (25)$$

$$\frac{\alpha_g}{\rho_g} \frac{\partial p}{\partial r} = -\frac{F_{td,r}}{\rho_g} - \frac{\partial \alpha_g \overline{u_r u_r^g}}{\partial r} + \frac{\alpha_g}{r} (\overline{u_\theta u_\theta^g} - \overline{u_r u_r^g}) \quad (26)$$

538

539 As anticipated in Ullrich et al. (2014), the pressure gradient can be eliminated to obtain an
 540 equation for the radial void fraction distribution:

541

$$\begin{aligned} \frac{\partial \alpha_g}{\partial r} \left[\frac{\rho_g}{\alpha_g} \overline{u_r u_r^g} + \frac{\rho_l}{\alpha_l} \overline{u_r u_r^l} \right] \\ = -\frac{F_{td,r}}{\alpha_g} - \frac{F_{td,r}}{\alpha_l} - \rho_g \frac{\partial \overline{u_r u_r^g}}{\partial r} + \rho_l \frac{\partial \overline{u_r u_r^l}}{\partial r} \\ + \frac{\rho_g}{r} (\overline{u_\theta u_\theta^g} - \overline{u_r u_r^g}) - \frac{\rho_l}{r} (\overline{u_\theta u_\theta^l} - \overline{u_r u_r^l}) \end{aligned} \quad (27)$$

542

543 Turbulence quantities are proportional to the phase density. In gas-liquid bubbly flows, where
 544 the density ratio ρ_g / ρ_l can be as low as 10^{-3} , the turbulence stresses in the gas phase can be
 545 neglected. Rearranging, the following equation can be obtained:

546

$$\alpha_g \frac{\partial \alpha_g}{\partial r} = -\frac{F_{td,r}}{\rho_l \overline{u_r u_r^l}} + \frac{\alpha_g (1 - \alpha_g)}{\overline{u_r u_r^l}} \left[\frac{\partial \overline{u_r u_r^l}}{\partial r} + \left(\frac{\overline{u_r u_r^l} - \overline{u_\theta u_\theta^l}}{r} \right) \right] \quad (28)$$

547

548 Clearly, from Eq. (28), turbulence in the liquid phase strongly impacts the phase distribution
 549 and is responsible for the preferential accumulation of bubbles near the wall in Figure 2 in the
 550 absence of lift and wall forces, with turbulent dispersion from Eq. (9) working against flow
 551 property gradients. More specifically, because of the very low density of the bubbles, the inertia
 552 of the bubbles is negligible with respect to the inertia of the fluid and turbophoresis is not
 553 sufficient to explain the wall-peaked void fraction profile. This is in contrast to solid particle
 554 flows, where the density of the dispersed phase is at least comparable and often higher than
 555 that of the carrier phase, such that the inertia of the particles and turbophoresis have a much
 556 more important impact on particle preferential distribution.

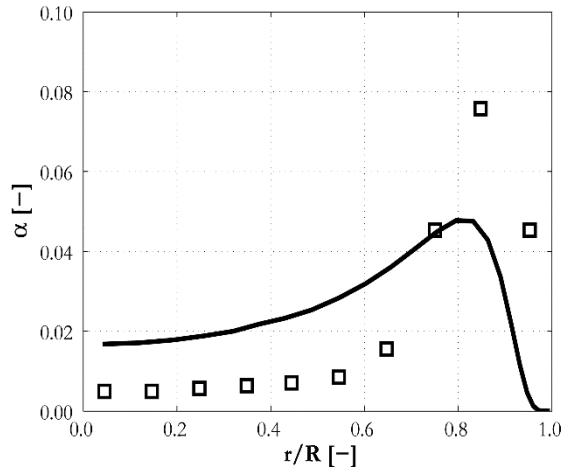
557

558 In gas-liquid bubbly flows, from Eq. (25) the continuous phase turbulence, and in particular
 559 the gradient in the radial turbulent stress, generates a radial pressure gradient in the flow. This
 560 pressure gradient pushes the bubbles towards the lower pressure region near the wall. There,
 561 pressure reaches a minimum and the subsequent increase as the wall is approached prevents
 562 the bubbles reaching the very near-wall region, shaping the wall-peaked void fraction profile
 563 of Figure 2. This effect is clearly visible in Figure 3, where the radial profile of the radial
 564 turbulent normal stress and the pressure are shown. Between the right-hand side terms in Eq.

565 (28), the first and second are dominant and comparable. Most importantly, a detailed
566 specification of the void fraction profile near the wall needs the turbulence field in that region
567 to be finely resolved. To do so, a turbulence model able to resolve the flow field down to the
568 viscous sub-layer is necessary. When this is the case, the peak in the void fraction distribution
569 can be predicted, as well as the subsequent decrease to zero towards the wall, even when
570 neglecting any repulsive force such as wall lubrication. These results are compared against
571 predictions of the high-Re turbulence models in Figure 4. Good accuracy is obtained using the
572 $k-\varepsilon$ and RSM models for the liquid mean velocity profile (Figure 4a). Distinctive features of
573 the void fraction profile (Figure 4b) are well-reproduced by all the models, although the high-
574 Re RSM is more accurate. However, the results obtained from the EB-RSM model suggest that
575 the impact of turbulence on the phase distribution is at least as significant as lift and wall
576 lubrication. Although radial changes in the pressure values are not dramatic (Figure 3b), the
577 small radial distance results in a significant contribution from the pressure gradient term in Eq.
578 (2). Its impact is comparable to that of the lift force (from high Reynolds number simulations)
579 away from the wall and reaches values as high as 50 N m^{-3} near the wall. In the near-wall region
580 itself, the pressure gradient contribution is significant when compared to that of the lift and
581 wall forces, which was observed to reach $80\text{-}90 \text{ N m}^{-3}$. It is, however, worth mentioning that
582 quantitative values of the lift and wall forces are unavoidably strongly coupled with each other
583 and arbitrarily related to the coefficients used in the respective models. It is possible that the
584 same void profile would have been obtained by reducing the contribution from both forces by
585 a similar amount.

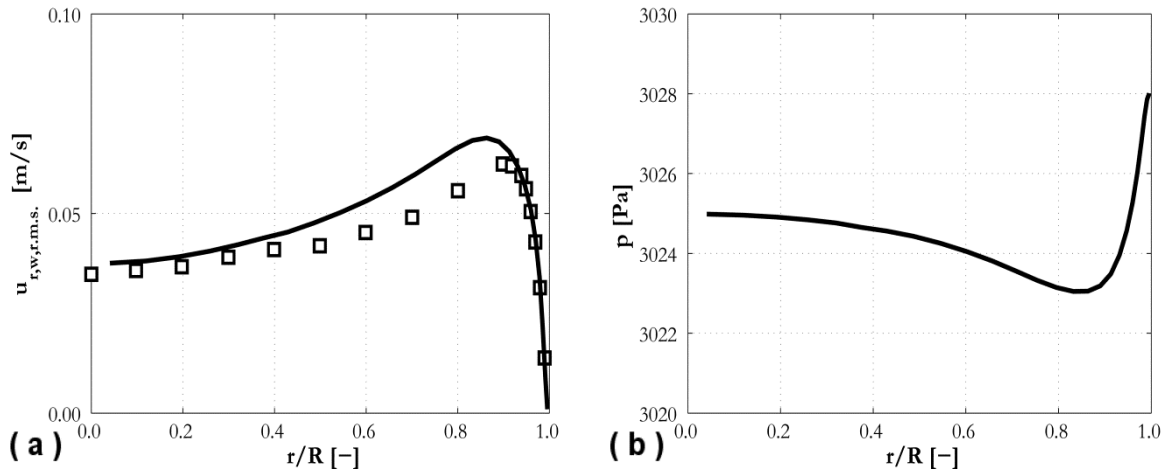
586
587 Comparison of the void fraction profiles from the high-Re $k-\varepsilon$ and RSM in Figure 4b confirms
588 the role of the pressure gradient. The impact of the lift force is similar between the two models.
589 However, the RSM model correctly predicts the radial pressure gradient, at least away from
590 the near-wall region, and shows a higher and more accurate peak. This suggests the EB-RSM
591 model can still be improved with the addition of a proper lift force contribution, which will be
592 investigated in the last section of this paper. Thanks to the resolution in the near-wall region,
593 however, the wall lubrication contribution required by the high-Re models seems unnecessary
594 with the EB-RSM model.

595



596
597
598
599

Figure 2. Radial void fraction profile using the EB-RSM model compared against the Hosokawa and Tomiyama (2009) experiment (\square data; — EB-RSM).



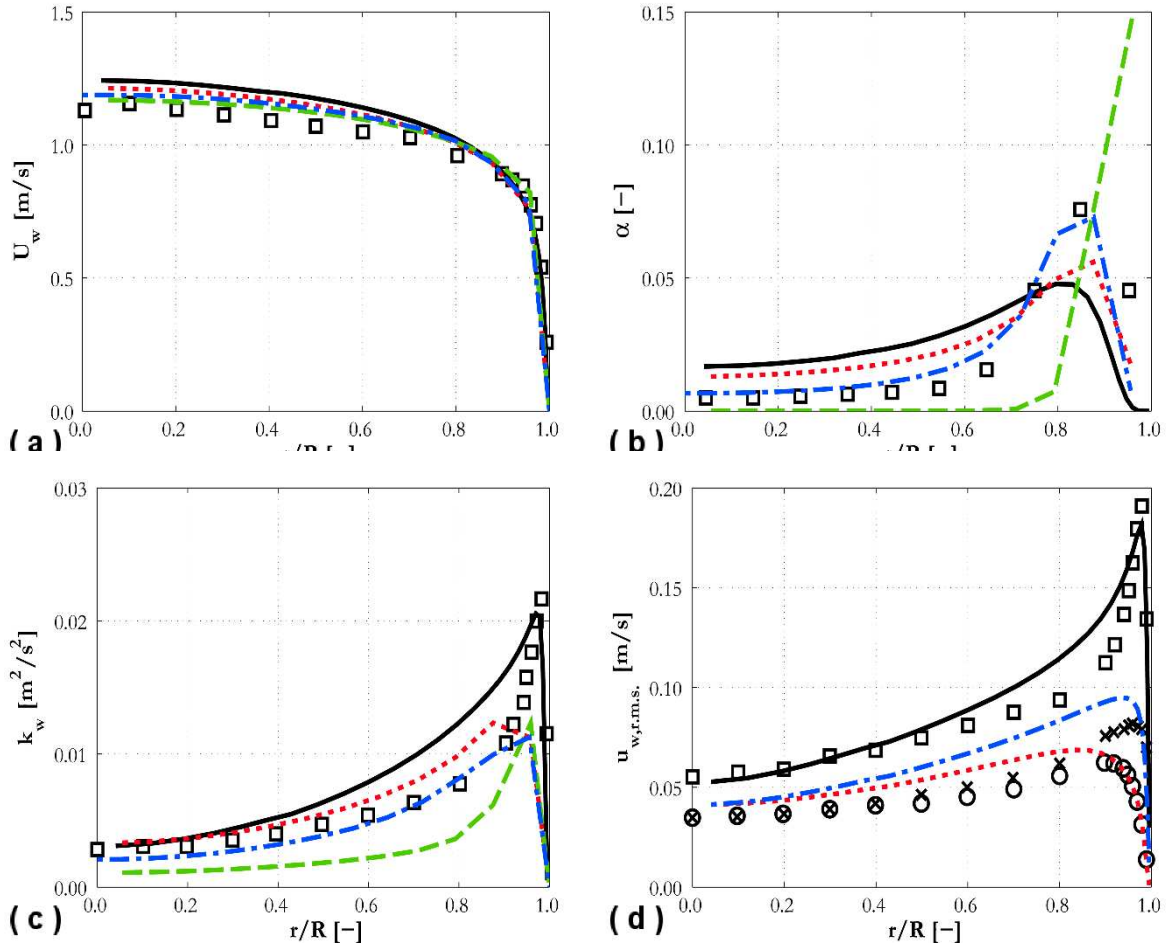
600
601
602
603

Figure 3. Radial variation of (a) r.m.s. of turbulent radial velocity fluctuations in water and (b) pressure using the EB-RSM model compared against the Hosokawa and Tomiyama (2009) experiment (\square data; — EB-RSM).

604
605
606
607
608
609
610
611
612
613

The near-wall capabilities of the EB-RSM are also shown in the accurate prediction of the peak in the turbulence kinetic energy near the wall in Figure 4c. Turbulence levels are well-predicted by including the contribution to turbulence from the bubbles. Anisotropy of the turbulence field and the behaviour of the turbulent stresses close to the wall are also well-predicted by the EB-RSM in Figure 4d, where radial profiles of the r.m.s. (root-mean-square) of the velocity fluctuations are compared against data from the Hosokawa and Tomiyama (2009) experiment. Good agreement is obtained, except for an overestimation of the azimuthal fluctuations in the near-wall region.

614



615

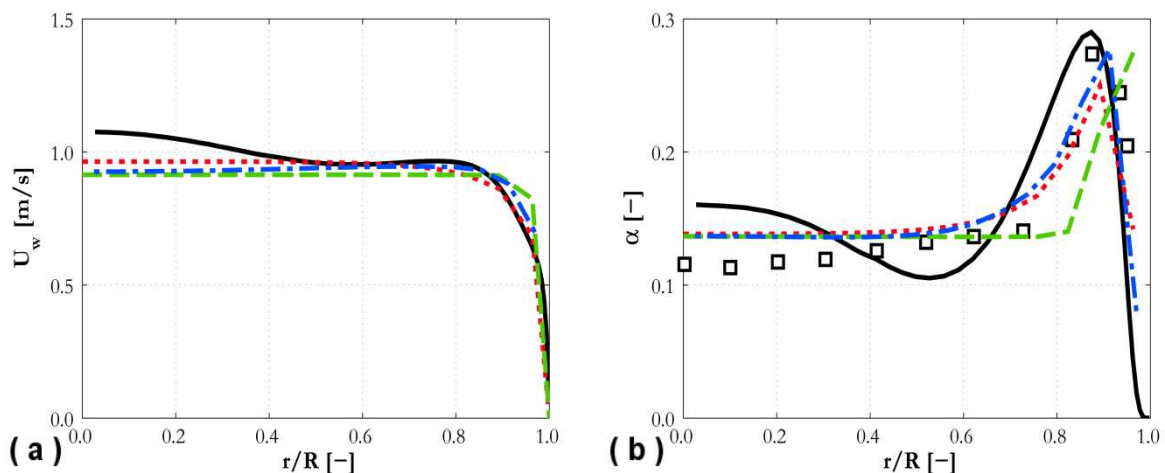
616 Figure 4. Radial predictions of (a) water mean axial velocity, (b) void fraction, (c) water
 617 turbulence kinetic energy and (d) r.m.s. of water velocity fluctuations compared against the
 618 Hosokawa and Tomiyama (2009) experiment (In (a)-(c): \square data; — EB-RSM; - - - RSM; ---
 619 $k - \varepsilon$; - - $k - \varepsilon$ with Tomiyama lift. In (d): EB-RSM predictions against data in: \square , — axial
 620 direction; \circ , --- radial direction; \times , - - - azimuthal direction).

621

622 In Figure 4, $k-\varepsilon$ results are shown for both a constant lift coefficient and the Tomiyama et al.
 623 (2002b) correlation. The constant lift model provides satisfactory accuracy, in line with
 624 experiments and other model predictions. In contrast, the Tomiyama et al. (2002b) correlation
 625 predicts too high a void fraction peak near the wall that rapidly diminishes to negligible values
 626 towards the centre of the pipe. The contribution of bubbles to the continuous phase turbulence
 627 in the latter region is therefore absent and, consequently, turbulence kinetic energy is under
 628 predicted. These findings confirm similar results reported in Colombo and Fairweather (2015).
 629 Therefore, and despite the relatively higher accuracy found for the other pipe flow experiment
 630 presented below, the Tomiyama et al. (2002b) model has not been used with the RSM, and in
 631 the following simulations with the $k-\varepsilon$ model.

632

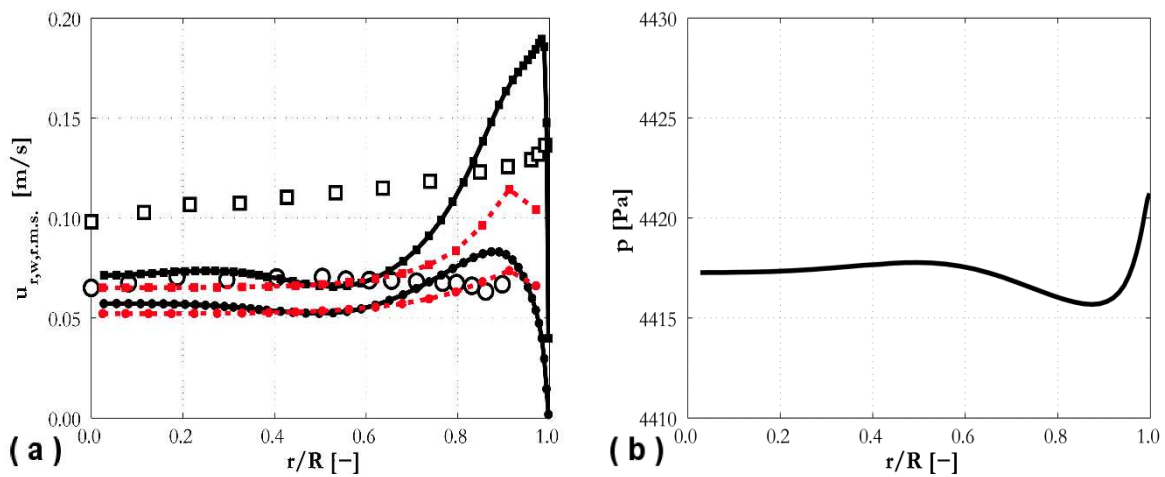
633 The Hosokawa and Tomiyama (2009) experiment was carried out at relatively low void
634 fraction. Therefore, comparisons were extended to a higher void fraction pipe flow using the
635 experiment data from Liu and Bankoff (1993a), with comparisons reported in Figure 5. Good
636 predictions of the peak in the void fraction are obtained with all the models considered.
637 However, in the centre of the pipe, the EB-RSM predicts a wavy behaviour in the void fraction
638 instead of the flat profile obtained with the alternative approaches. Although not completely
639 flat, the experimental data confirm the high Reynolds number results. An increase in the liquid
640 mean velocity towards the centre of the pipe predicted by the EB-RSM reflects the similar
641 increase in the void fraction, whilst the other models again predict a flat velocity profile.
642 Unfortunately, no experimental data on the liquid mean velocity are available for this
643 experiment. Although the behaviour towards the centre of the pipe is not well-predicted by the
644 EB-RSM, the qualitative features of a wall-peaked void fraction profile are again obtained
645 without considering the lift and wall lubrication contributions. As noted, better results are
646 shown by the other models in regards to the void fraction towards the centre of the pipe,
647 including that based on the Tomiyama et al. (2002b) approach, although the near-wall peak
648 obtained using the latter is not in agreement with the data. As already mentioned, because of
649 inconsistencies in the results obtained with the Tomiyama et al. (2002b) model, it was not used
650 with the RSM or in all other following simulations using the $k-\varepsilon$ turbulence model.
651



652 **(a)** **(b)**
653 Figure 5. Radial predictions of (a) water mean axial velocity and (b) void fraction compared
654 against the Liu and Bankoff (1993a) experiment (\square data; — EB-RSM; - - - RSM; --- $k-\varepsilon$;
655 - - $k-\varepsilon$ with Tomiyama lift).
656

657 Turbulence generates a radial pressure gradient (Figure 6), similar to that observed in the
658 Hosokawa and Tomiyama experiment (2009), which is responsible for the bubble preferential

659 accumulation. Comparisons between data and EB-RSM predictions for the radial profiles of
 660 the streamwise and radial r.m.s. of the velocity fluctuations are also given in this figure.
 661 Although turbulence anisotropy is predicted, the accuracy is not as high as for the low void
 662 fraction case (Figure 4). More specifically, the streamwise turbulent fluctuations are under
 663 predicted in the centre of the pipe and over predicted in the near-wall region. For comparison,
 664 the high-Re RSM predictions are also included in Figure 6a. Similar discrepancies are found,
 665 although the high-Re RSM also under predicts the streamwise r.m.s. in the near-wall region.
 666 The radial pressure profile shows a low-pressure region near the wall, with the pressure initially
 667 increasing but then slightly decreasing again in moving towards the pipe centre. This decrease
 668 promotes void fraction accumulation near the pipe centre. It is difficult to assess whether this
 669 occurs due to the absence of other momentum transfer terms, such as those due to lift and wall
 670 forces, or to inaccuracies in the prediction of the turbulence field. The effect on the oscillating
 671 behaviour of the addition of other radial forces such as lift is investigated further below.
 672



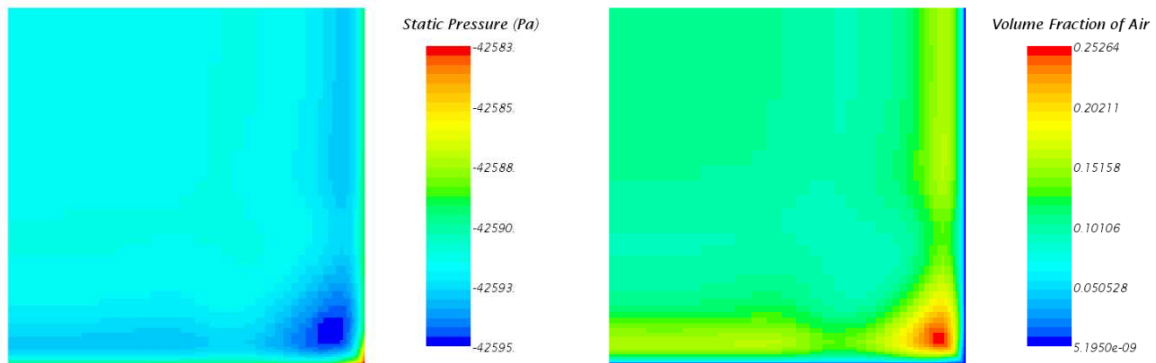
673 (a) 674 Figure 6. Radial predictions of (a) r.m.s. of turbulent radial velocity fluctuations in water and
 675 (b) pressure compared against the Liu and Bankoff (1993a) experiment (In (a): \square axial
 676 direction; \circ radial direction; — EB-RSM; --- RSM).
 677

678 4.2. Square duct

679 Previous research has mostly focused on pipe flows, and it is therefore interesting to extend the
 680 present analysis to other geometrical configurations, such as the square duct flow studied
 681 experimentally by Sun et al. (2014). Cross-sectional views of the pressure and void fraction
 682 distribution predicted by the EB-RSM are given in Figure 7, which shows a 1/4 cross-sectional
 683 view of the square duct. Similarly to what occurs in pipes, the pressure is lower in the near-
 684 wall region with respect to the centre of the duct. The pressure is at a minimum in the corner
 685

686 of the duct. Driven by the pressure, the void fraction peaks along the two lateral walls and has
687 a distinctive maximum in the corner.

688



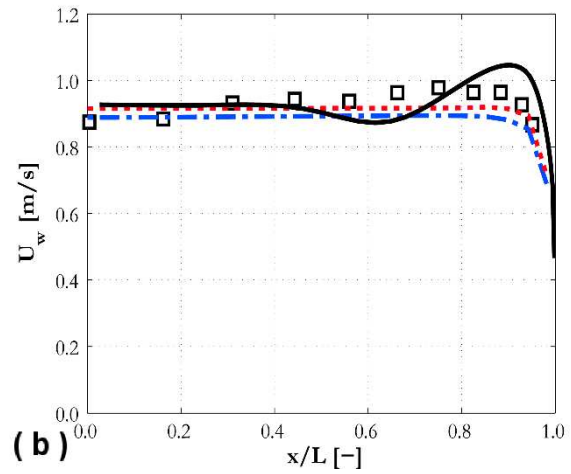
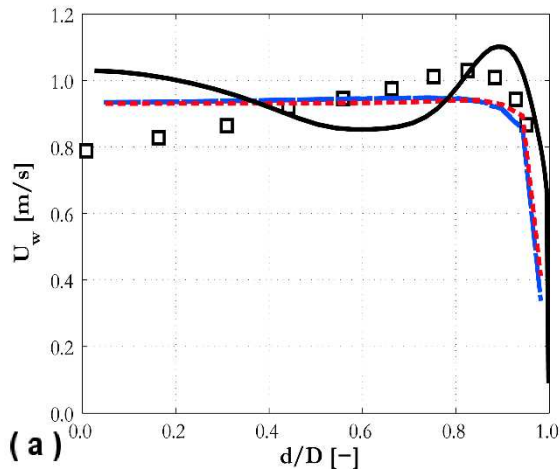
689

690 Figure 7. Pressure (left) and void fraction (right) in the square duct cross-section calculated
691 using the EB-RSM model.

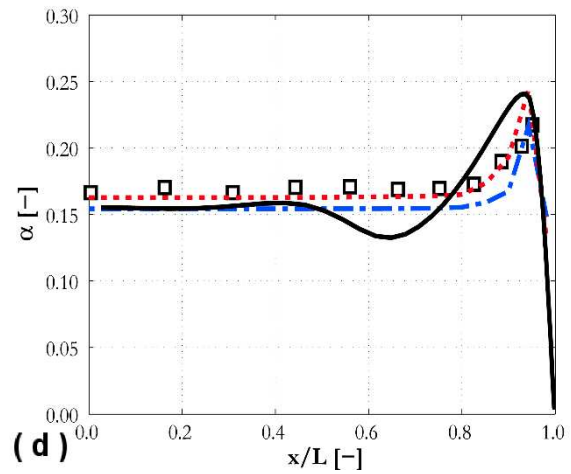
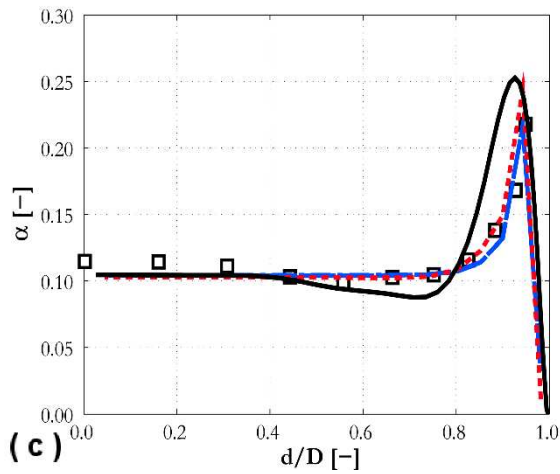
692

693 Void fraction (and pressure) distributions in the near-wall region are predicted in great detail
694 due to the fine resolution near the walls allowed by the EB-RSM. Comparison of predictions
695 with experimental data is given in Figure 8 for data gathered on the duct diagonal and on a line
696 parallel to the duct wall (in the plots, results are presented as a function of the distance from
697 the centre line along the diagonal d normalized by the diagonal half-length D , and the distance
698 from the centre on a line parallel to the wall x normalized by the duct side half-length L).
699 Predictions of the RSM and $k-\varepsilon$ models are also included. Velocity and void fraction profiles
700 from the EB-RSM show the same wavy behaviour already noted above, with an increase in the
701 void fraction and, consequently, of the liquid mean velocity occurring towards the centre of the
702 duct. In contrast, the RSM and $k-\varepsilon$ based model predictions show a flat mean velocity profile
703 away from the duct walls, and a wall-peaked void profile that becomes flat towards the duct
704 centre. Agreement with experiment is good using the same lift and wall force models employed
705 for the pipe flows considered earlier. The EB-RSM predicts the near-wall peak in the velocity
706 profiles, unlike the other models, and the peaks in the void fraction profiles with reasonable
707 accuracy. On the duct diagonal, the EB-RSM is also the only model to predict the slight
708 decrease in void fraction after the near-wall peak and the subsequent increase towards the
709 centre of the duct. However, the drop in velocity and void fraction after the peaks is generally
710 over predicted, and in some cases not supported by experimental evidence. The EB-RSM also
711 predicts excessive turbulence kinetic energy near the duct wall but, in the centre of the duct,
712 agreement with data is comparable to that of the other models on the diagonal and significantly
713 improved parallel to the wall. Overall, all the models demonstrate a reasonable accuracy.

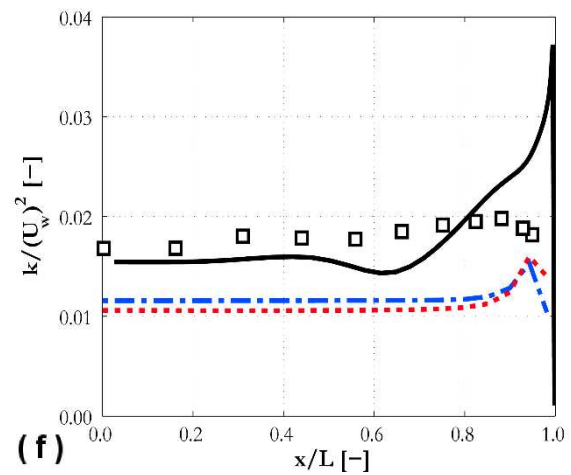
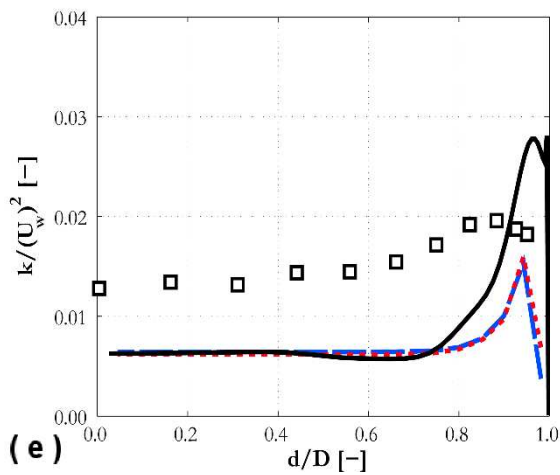
714



715



716

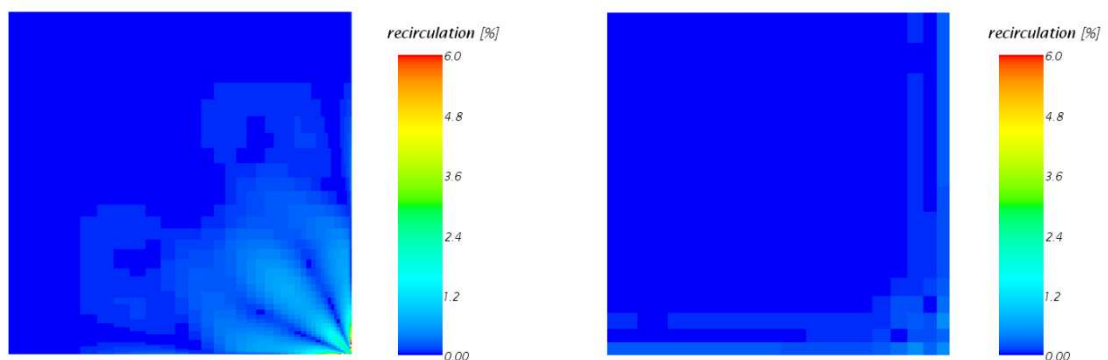


717 Figure 8. Predictions of (a, b) water mean axial velocity, (c, d) void fraction and (e, f)
 718 turbulence kinetic energy compared against the Sun et al. (2014) experiment. Profiles are
 719 shown on the diagonal (a, c and e, where d is the distance from the centre line along the
 720 diagonal and D the diagonal half-length) and on a line parallel to the wall (b, d and f, where x
 721 is the distance along a line from the central plane perpendicular to the line and L the duct half
 722 side length) (\square data; — EB-RSM; - - - RSM; --- $k - \varepsilon$).

723

724 The results in Figure 8 demonstrate how distinctive features of the flow in a square duct can be
 725 reproduced, even when lift and wall lubrication forces are neglected. Discrepancies are

726 observed towards the centre of the duct, with a wavy behaviour of the void fraction and velocity
727 profiles that was also observed in the pipe flow of Liu and Bankoff (1993a). As noted earlier,
728 the presence of additional interfacial forces such as lift may smooth out this wavy behaviour.
729 It is worth mentioning that the aim at this stage is not to prove that the pressure gradient is the
730 only determinant of the radial void fraction distribution, because the lift force also plays a major
731 role. However, the impact of the multiphase turbulence field and the induced pressure field are
732 comparable and need to be properly accounted for to permit accurate modelling. An additional
733 interesting aspect is depicted in Figure 9, which shows flow recirculation in the same quarter
734 of the duct cross-section used in Figure 8. Recirculation is presented as a percentage of the
735 ratio between the cross-sectional velocity magnitude and the streamwise velocity. It is well-
736 known how the anisotropy of the turbulence field in ducts generates recirculation zones in
737 single-phase flows (Brundrett, 1964; Sun et al., 2014), with two counter-rotating vortices in
738 each duct corner. This recirculation is normally well-predicted in single-phase flow by using
739 Reynolds stress turbulence models. Corner recirculation, which amounts to around 2% of the
740 mean streamwise velocity, is predicted by the EB-RSM model. In the left hand side of Figure
741 9, recirculation is clearly visible in the lower right corner of the figure that identifies the corner
742 in the 1/4 duct cross-section. However, in the same cross-section, recirculation is not predicted
743 by the high-Re RSM that includes lift and wall lubrication forces (right hand side of Figure 9).
744 Even though observations in single-phase flows support the presence of a recirculation pattern,
745 unfortunately no measurements are available for two-phase bubbly flows and additional
746 experimental work on such flows is therefore necessary to further elucidate this specific topic.
747



748
749 Figure 9. Secondary flow in the square duct cross-section calculated using the EB-RSM and
750 the high Reynolds number RSM (left to right).
751
752
753

754 **4.3. Rod bundles**

755

756 With respect to the previous cases considered, rod bundles involve a much more complicated
757 flow pattern that includes mixing and recirculation between the channels. Therefore, testing of
758 CFD models against data on rod bundles is interesting and challenging, and of particular
759 relevance when addressing nuclear reactor thermal-hydraulics flows. Profiles of water and gas
760 mean velocities, void fraction and the r.m.s of velocity fluctuations are presented in Figure 10
761 for the experiment of Hosokawa et al. (2014), where x represents the distance from the wall of
762 the channel box on a line perpendicular to the wall and L is the side half-length of the box.
763 Cross-sectional distributions of the void fraction are shown in Figure 11.

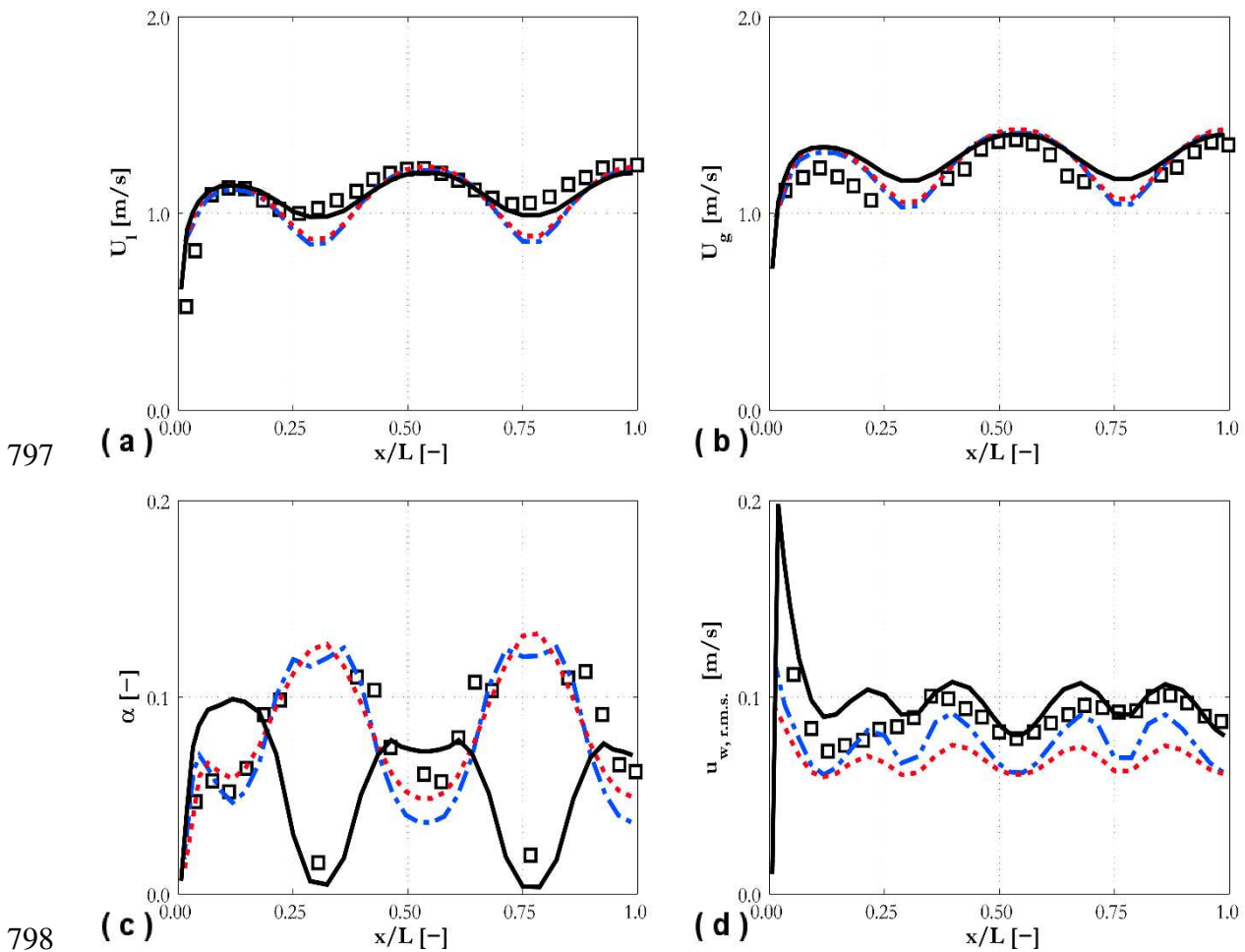
764

765 None of the models successfully predicts the void fraction distribution. In Figure 11, the RSM
766 and $k-\varepsilon$ model predictions shows peaks in the void fraction distribution in the gaps between
767 two neighbouring rods. In contrast, experimental measurements show a minimum in the void
768 fraction distribution in the same regions (Hosokawa et al., 2014). The void fraction distribution
769 in the sub-channels is well-predicted, as confirmed by the profiles in Figure 10. These profiles
770 correspond to a vertical line between the rods in Figure 11. In Figure 11, where the experiments
771 show a minimum, the RSM and $k-\varepsilon$ model predictions show maximum values of the void
772 fraction. Similarly, from Hosokawa et al. (2014), the corner region in Figure 11 is a low void
773 fraction region, whereas these models predict the maximum value of the void fraction to be
774 located in the corner. Therefore, although the coefficients appearing in the lift and wall force
775 models have been tested and validated over a wide range of flow conditions in pipes and in a
776 square channel, the same coefficients are not entirely applicable when much more complex
777 geometries such as a rod bundle are considered. On the other hand, the minimum void regions
778 are well-reproduced by the EB-RSM, although the void fraction distribution in the sub-
779 channels is not predicted with any degree of accuracy, this probably being due to it not
780 accounting for any other interfacial force other than the turbulent dispersion. It must also be
781 remembered that, although bubbles are not rigid spheres and can deform, the minimum void
782 fraction regions were attributed by Hosokawa et al. (2014) to geometrical constraints rather
783 than flow conditions. By including confinement effects in the closure models, the authors were
784 indeed able to improve the accuracy of their model. Therefore, further validation against
785 experiments using smaller bubbles, whose preferential distribution is not affected by any
786 geometrical constraints, is desirable.

787

788 Velocity profiles are in reasonable agreement with experiment for all the three models,
 789 although the EB-RSM provides a more accurate estimation of the liquid velocity in the gaps
 790 between neighbouring rods. Consequently, the bubble velocity is over predicted in the same
 791 regions. However, this might not have a significant effect on the flow since practically no
 792 bubbles are found in these regions. Similarly to the square duct case, the EB-RSM predicts
 793 higher turbulence levels which are more in agreement with experimental data. In the wall
 794 region, however, the EB-RSM may be over predicting the turbulence peak, even if detailed
 795 measurements are not available in this region.

796



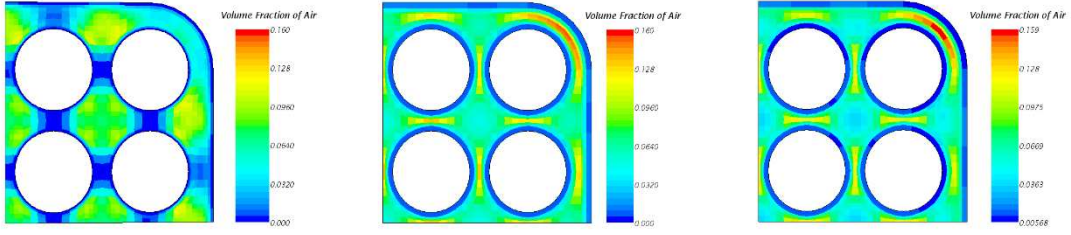
798

799 Figure 10. Predictions of (a) water mean velocity, (b) bubble mean velocity, (c) void fraction
 800 and (d) r.m.s. of streamwise water velocity fluctuations compared against the Hosokawa et al.
 801 (2014) experiment in a 4×4 rod bundle ((\square) data; — EB-RSM; --- RSM; --- $k - \varepsilon$). In the
 802 plots, x is the distance from the wall of the channel box along a line perpendicular to the wall
 803 and L is the side half-length of the box.

804

805

806



807

808

Figure 11. Void fraction distribution in the rod bundle cross-section calculated with the EB-RSM, RSM and $k-\epsilon$ models, respectively (left to right).

809

810

811 5. Lift force modelling with the EB-RSM

812

813

814

815

816

817

818

819

820

821

822

823

824

825

826

827

$$C_L = \begin{cases} 0 & y_w/d_B < 0.5 \\ C_{L0} \left[3 \left(2 \frac{y_w}{d_B} - 1 \right)^2 - 2 \left(2 \frac{y_w}{d_B} - 1 \right)^3 \right] & 0.5 \leq y_w/d_B \leq 1 \\ C_{L0} & y_w/d_B > 1 \end{cases} \quad (29)$$

828

829

830

831

832

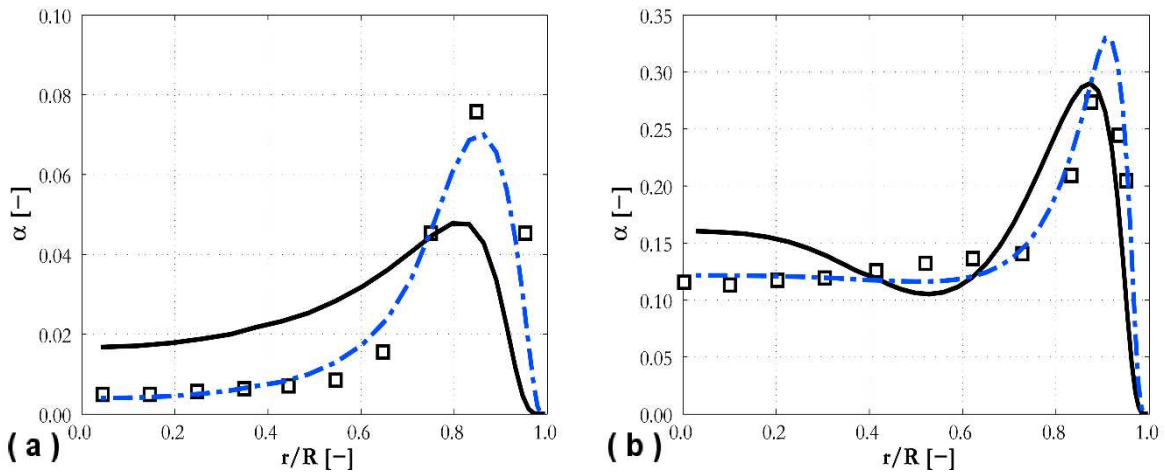
833

834

835

The value of the lift coefficient C_{L0} has been kept equal to 0.1, consistently with the lift coefficient used for the high-Reynolds turbulence models. Comparisons for the EB-RSM with and without the lift contribution are shown in Figure 12 for the pipe flows of Hosokawa and Tomiyama (2009), Figure 12a, and Liu and Bankoff (1993a), Figure 12b. The accuracy of the model is remarkable and the impact of lift significant. The wall-peak is well predicted and the addition of lift removes the wavy behaviour in the void fraction in the centre of the pipe. It is worth mentioning that the model in Eq. (29) was also adopted in the recent work of Lubchenko

836 et al. (2018). However, the latter authors introduced a modification in the turbulent dispersion
 837 force to reproduce the void peak in the absence of any wall lubrication contribution. Otherwise,
 838 the void profile remained flat after the peak and towards the wall. In contrast, the resolution of
 839 the near-wall region by the EB-RSM allows reproduction of the wall peak without any
 840 additional modification.
 841

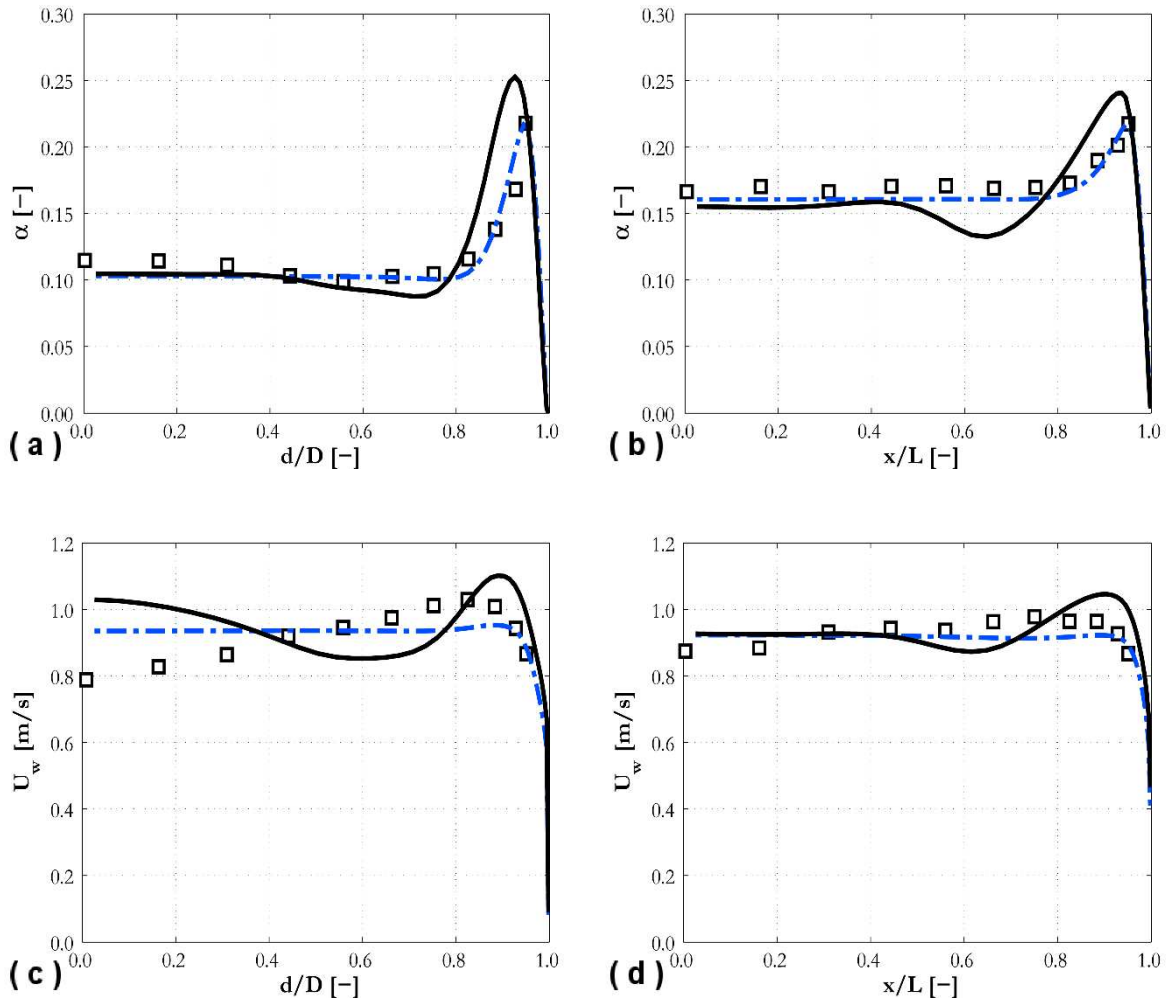


842 **(a)** Figure 12. Void fraction profiles for (a) Hosokawa and Tomiyama (2009) and (b) Liu and
 843 Bankoff (1993a) experiments (\square data; — EB-RSM; - - - EB-RSM with lift).
 844
 845

846 Void fraction and velocity profiles for the square duct on the diagonal and parallel to the duct
 847 wall are presented in Figure 13. The accuracy of the void fraction distribution is improved and
 848 the wavy behaviour in the void fraction and velocity in the centre of the duct, which is a major
 849 drawback when lift is not accounted for, is no longer apparent when lift is included. With the
 850 addition of the lift force, flat velocity profiles similar to those predicted with the high-Re
 851 models in Figure 8 are obtained, although the velocity peak in the corner of the duct is under
 852 predicted to some extent. In the experiments, larger bubbles were found in the corner region.
 853 Therefore, improvements can be expected with the addition of a population balance model able
 854 to correctly predict the distribution of the bubble diameter in the duct cross-section.
 855

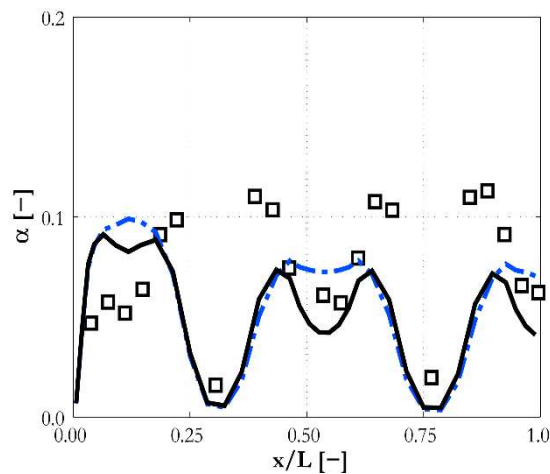
856 Finally, the void fraction distribution in the rod bundle is shown in Figure 14 for the EB-RSM
 857 model with and without lift. In this case, quantitative improvement is not obtained, except for
 858 a small portion of the profile at x/L around 0.5. However, the accurate prediction of negligible
 859 void fraction in the spaces between the rods is maintained.
 860
 861

862
863



864

865 Figure 13. Predictions of (a, b) void fraction and (c, d) water mean velocity compared against
866 the Sun et al. (2014) experiment. Profiles are shown on the diagonal (a, c) and on a line
867 parallel to the wall (b, d) (\square data; — EB-RSM; - - - EB-RSM with lift).
868



869

870 Figure 14. Predictions of void fraction compared against the Hosokawa et al. (2014)
871 experiment in a 4×4 rod bundle ((\square data; — EB-RSM; - - - EB-RSM with lift).
872
873

874 6. Conclusions

875

876 Bubbly flows have been predicted with an Eulerian-Eulerian CFD two-fluid model closed
877 using three turbulence models. High Reynolds number $k-\varepsilon$ and RSM approaches, which
878 represent current best-practice in industry and often research, using RANS approaches at least,
879 are compared with an EB-RSM that resolves the near-wall region. The high Reynolds number
880 models employed a common set of closures for momentum transfer, with mainly lift and wall
881 lubrication forces determining the lateral void fraction distribution. However, lift and wall
882 lubrication forces are neglected within the EB-RSM, with only drag and turbulent dispersion
883 considered. The EB-RSM turbulence model has also been improved with the addition of a
884 bubble-induced turbulence contribution to successfully predict the continuous phase turbulence
885 field in bubbly flows. Other than for the normal pipe geometry, the accuracy of the models was
886 additionally tested in square duct and rod bundle flows.

887

888 The main features of the flows and the void fraction distribution are well-reproduced by all
889 three models, and even by the EB-RSM that does not account for lift and wall lubrication
890 forces. Overall, good agreement against data is obtained, except for the rod bundle experiment.
891 Therefore, the lift and wall force models, although having been extensively validated in pipe
892 flows, and showing good accuracy in the square duct, are not easily extendable to a more
893 complex geometry such as a rod bundle. Additionally, even if the accuracy of model
894 predictions is unsatisfactory in this case, the EB-RSM predicts features of the flow which are
895 not reproduced by the other two models.

896

897 As demonstrated by the EB-RSM predictions, the turbulence structure in the continuous phase
898 and the induced lateral pressure distribution have a strong effect on the lateral void fraction
899 distribution. The lift force still has a significant impact, and substantial improvements are
900 obtained when it is added to the EB-RSM based predictions. In contrast, the wall lubrication
901 model is unnecessary when the near-wall region is properly resolved. Overall, the present
902 results suggest the action of turbulence has to be accurately taken into account and the near-
903 wall region properly modelled to improve the accuracy and reliability of two-fluid models.
904 Second-moment closures are to be preferred to two-equation, eddy viscosity-based approaches
905 and, specifically, major improvements can be expected from the development of near-wall
906 treatments specifically designed for two-phase flows. The present model can be used as the
907 basis for further improving the accuracy and general applicability of CFD two-fluid models.

908 Inaccuracies in the prediction of the rod bundle flow suggest further improvement of the lift
 909 model that is used with the EB-RSM is necessary. Extension of the lift model to cap-bubbles,
 910 and the addition of a population balance model, will be the subject of further work to extend
 911 the model to poly-dispersed bubbly flows.

912

913 **Acknowledgements**

914

915 The authors gratefully acknowledge the financial support of the EPSRC under grant
 916 EP/M018733/1, Grace Time, part of the UK-India Civil Nuclear Collaboration.

917

918 **Nomenclature**

919

920	a	anisotropy tensor [-]
921	C_D	drag coefficient [-]
922	C_L	lift coefficient [-]
923	D	diagonal [m]
924	D_h	hydraulic diameter [m]
925	D_R	Reynolds stress diffusion flux [$\text{J m}^{-2} \text{s}^{-1}$]
926	d	distance from the duct corner
927	d_B	bubble diameter [m]
928	E	bubble aspect-ratio [-]
929	Eo	Eötvös number ($\Delta\rho g d_B / \sigma$) [-]
930	F_d	drag force [N]
931	F_{td}	turbulent dispersion force
932	F_w	wall force
933	g	gravitational acceleration [m s^{-2}]
934	k	turbulence kinetic energy [$\text{m}^2 \text{s}^{-2}$]
935	j	superficial velocity [m s^{-1}]
936	L	length [m]
937	L_t	turbulent length scale [m]
938	M	interfacial momentum transfer source [N m^{-3}]
939	Mo	Morton number ($g\mu c 4\Delta\rho / \rho_c^2 \sigma^3$) [-]
940	P, P_k	production of shear-induced turbulence kinetic energy [$\text{J m}^{-3} \text{s}^{-1}$]
941	p	pressure [Pa]
942	r	radial coordinate [m]
943	R	radius [m]
944	R_{ij}	turbulent stress [$\text{m}^2 \text{s}^{-2}$]
945	Re_B	bubble Reynolds number ($\rho_c U_r d_B / \mu_c$) [-]
946	r	radial coordinate [m]
947	S	strain rate [s^{-1}]
948	S^{BI}	bubble-induced turbulence source term [$\text{J m}^{-3} \text{s}^{-1}$]
949	t	time [s]
950	U	velocity [m s^{-1}]
951	U_r	relative velocity [m s^{-1}]
952	u	instantaneous turbulence velocity fluctuation [m s^{-1}]
953	x	spatial coordinate [m]
954	y_w	wall distance [m]
955	W	rotation rate tensor [s^{-1}]

956

957 **Greek symbols**

958	α	volume fraction [-]
959	α_{EB}	elliptic-blending function [-]
960	ε	turbulence dissipation rate [m^2s^{-3}]
961	μ	molecular dynamic viscosity [Pa·s]
962	μ_t	turbulent dynamic viscosity [Pa·s]
963	ν_t	turbulent kinematic viscosity [m^2s]
964	ρ	density [$kg\ m^{-3}$]
965	σ	surface tension [$N\ m^{-1}$]
966	$\sigma_\alpha, \sigma_k, \sigma_\varepsilon$	turbulent Prandtl number for the void fraction, turbulence kinetic energy and
967		turbulence dissipation rate [-]
968	τ	laminar stress tensor [Pa]
969	τ^{Re}	turbulent stress tensor [Pa]
970	τ_{BI}	bubble-induced turbulence timescale [s]
971	Φ	pressure-strain correlation [m^2s^{-3}]

972

973

974 **Subscripts**

975

976	a	air
977	c	continuous phase
978	d	dispersed phase
979	g	gas
980	k	phase k
981	l	liquid
982	r	radial direction
983	w	water
984	θ	angular direction

985

986 **Superscripts**

987

988	g	gas
989	h	standard away from the wall model
990	l	liquid
991	w	wall model

992

993 **Declaration of interests**

994

995 None

996

997 **References**

998

999 Antal, S.P., Lahey, R.T., Flaherty, J.E., 1991. Analysis of phase distribution in fully developed
1000 laminar bubbly two-phase flow. *International Journal of Multiphase Flow* 17, 635-652.

1001

1002 Behzadi, A., Issa, R.I., Rusche, H., 2004. Modelling of dispersed bubble and droplet flow at
1003 high phase fractions. *Chemical Engineering Science* 59, 759-770.

1004

1005 Besagni, G., Guedon, G.R., Inzoli, F., 2018. Computational fluid-dynamic modeling of the
1006 mono-dispersed homogeneous flow regime in bubble columns. *Nuclear Engineering and*
1007 *Design* 331, 222-237.
1008

1009 Brundrett, E., 1964. The production and diffusion of vorticity in duct flow. *Journal of Fluid*
1010 *Mechanics* 19, 375-394.
1011

1012 Burns, A.D., Frank, T., Hamill, I., Shi, J.M., 2004. The Favre averaged drag model for turbulent
1013 dispersion in Eulerian multi-phase flows, Fifth International Conference on Multiphase Flows,
1014 Yokohama, Japan, May 30 - June 4.
1015

1016 CD-adapco, 2016. STAR-CCM+® Version 10.04 User Guide.
1017

1018 Clift, R., Grace, J.R., Weber, M.E., 1978. *Bubbles, drops and particles*. Academic Press, New
1019 York.
1020

1021 Coddington, P., Macian, R., 2002. A study of the performance of void fraction correlations
1022 used in the context of drift-flux two-phase flow models. *Nuclear Engineering and Design* 215,
1023 199-216.
1024

1025 Colombo, M., Fairweather, M., 2015. Multiphase turbulence in bubbly flows: RANS
1026 simulations. *International Journal of Multiphase Flow* 77, 222-243.
1027

1028 Colombo, M., Fairweather, M., 2016. RANS simulation of bubble coalescence and break-up
1029 in bubbly two-phase flows. *Chemical Engineering Science* 146, 207-225.
1030

1031 Dabiri, S., Tryggvason, G., 2015. Heat transfer in turbulent bubbly flow in vertical channel.
1032 *Chemical Engineering Science* 122, 106-113.
1033

1034 Daly, B.J., Harlow, F.H., 1970. Transport equations of turbulence. *Physics of Fluids* 13, 2634-
1035 2649.
1036

1037 Drew, D.A., Lahey Jr., R.T., 1982. Phase-distribution mechanisms in turbulent low-quality
1038 two-phase flow in a circular pipe. *Journal of Fluid Mechanics* 117, 91-106.
1039

1040 Ervin, E.A., Tryggvason, G., 1997. The rise of bubbles in a vertical shear flow. *Journal of*
1041 *Fluids Engineering* 119, 443-449.
1042

1043 Feng, J., Bolotnov, I.A., 2017. Evaluation of bubble-induced turbulence using direct numerical
1044 simulation. *International Journal of Multiphase Flow* 93, 92-107.
1045

1046 Gosman, A.D., Lekakou, C., Politis, S., Issa, R.I., Looney, M.K., 1992. Multidimensional
1047 modeling of turbulent two-phase flows in stirred vessels. *AIChE Journal* 38, 1946-1956.
1048

1049 Hassan, Y.A., 2014. Full-field measurements of turbulent bubbly flow using innovative
1050 experimental techniques. CASL Technical Report, CASL-U-2014-0209-000.
1051

1052 Hibiki, T., Ishii, M., 2007. Lift force in bubbly flow systems. *Chemical Engineering Science*
1053 62, 6457-6474.
1054

1055 Hosokawa, S., Hayashi, K., Tomiyama, A., 2014. Void distribution and bubble motion in
1056 bubbly flows in a 4×4 rod bundle. Part I: Experiments. *Journal of Nuclear Science and*
1057 *Technology* 51, 220-230.

1058
1059 Hosokawa, S., Tomiyama, A., 2003. Lateral force acting on a deformed single bubble due to
1060 the presence of a wall. *Transactions of the JSME* 69, 2214-2220.

1061
1062 Hosokawa, S., Tomiyama, A., 2009. Multi-fluid simulation of turbulent bubbly pipe flow.
1063 *Chemical Engineering Science* 64, 5308-5318.

1064
1065 Jones, W.P., Launder, B.E., 1972. The prediction of laminarization with a two-equation model
1066 of turbulence. *International Journal of Heat and Mass Transfer* 15, 301-314.

1067
1068 Kataoka, I., Serizawa, A., 1989. Basic equations of turbulence in gas-liquid two-phase flow.
1069 *International Journal of Multiphase Flow* 15, 843-855.

1070
1071 Kim, M., Lee, J.H., Park, H., 2016. Study of bubble-induced turbulence in upward laminar
1072 bubbly pipe flows measured with a two-phase particle image velocimetry. *Experiments in*
1073 *Fluids* 57, 55.

1074
1075 Lahey, R.T., Drew, D.A., 2001. The analysis of two-phase flow and heat transfer using a
1076 multidimensional, four field, two-fluid model. *Nuclear Engineering and Design* 204, 29-44.

1077
1078 Lahey, R.T., Lopez de Bertodano, M., Jones Jr, O.C., 1993. Phase distribution in complex
1079 geometry conduits. *Nuclear Engineering and Design* 141, 177-201.

1080
1081 Liao, Y., Lucas, D., 2010. A literature review on mechanisms and models for the coalescence
1082 process of fluid particles. *Chemical Engineering Science* 65, 2851-2864.

1083
1084 Liao, Y., Rzehak, R., Lucas, D., Krepper, E., 2015. Baseline closure model for dispersed
1085 bubbly flow: Bubble coalescence and breakup. *Chemical Engineering Science* 122, 336-349.

1086
1087 Liu, T.J., Bankoff, S.G., 1993a. Structure of air-water bubbly flow in a vertical pipe - I. Liquid
1088 mean velocity and turbulence measurements. *International Journal of Heat and Mass Transfer*
1089 36, 1049-1060.

1090
1091 Liu, T.J., Bankoff, S.G., 1993b. Structure of air-water bubbly flow in a vertical pipe - II. Void
1092 fraction, bubble velocity and bubble size distribution. *International Journal of Heat and Mass*
1093 *Transfer* 36, 1061-1072.

1094
1095 Lopez de Bertodano, M., Lahey, R.T., Jones, O.C., 1994. Phase distribution in bubbly two-
1096 phase flow in vertical ducts. *International Journal of Multiphase Flow* 20, 805-818.

1097
1098 Lopez de Bertodano, M., Lee, S.J., Lahey Jr., R.T., Drew, D.A., 1990. The prediction of two-
1099 phase turbulence and phase distribution phenomena using a Reynolds stress model. *Journal of*
1100 *Fluids Engineering* 112, 107-113.

1101
1102 Lu, J., Tryggvason, G., 2013. Dynamics of nearly spherical bubbles in a turbulent channel
1103 upflow. *Journal of Fluid Mechanics* 732, 166-189.

1104 Lubchenko, N., Magolan, B., Sugrue, R., Baglietto, E., 2018. A more fundamental wall
1105 lubrication force from turbulent dispersion regularization for multiphase CFD applications.
1106 International Journal of Multiphase Flow 98, 36-44.
1107

1108 Lucas, D., Beyer, M., Szalinski, L., Schutz, P., 2010. A new databse on the evolution of air-
1109 water flows along a large vertical pipe. International Journal of Thermal Sciences 49, 664-674.
1110

1111 Manceau, R., 2015. Recent progress in the development of the elliptic blending Reynolds-stress
1112 model. International Journal of Heat and Fluid Flow 51, 195-220.
1113

1114 Manceau, R., Hanjalic, K., 2002. Elliptic blending model: A new near-wall Reynolds-stress
1115 turbulence closure. Physics of Fluids 14, 744-754.
1116

1117 Mimouni, S., Archambeau, F., Boucker, M., Lavieville, J., Morel, C., 2010. A second order
1118 turbulence model based on a Reynolds stress approach for two-phase boiling flows. Part 1:
1119 Application to the ASU-annular channel case. Nuclear Engineering and Design 240, 2233-
1120 2243.
1121

1122 Mimouni, S., Lavieville, J., Seiler, N., Ruyer, P., 2011. Combined evaluation of second order
1123 turbulence model and polydispersion model for two-phase boiling flow and application to fuel
1124 assembly analysis. Nuclear Engineering and Design 241, 4523-4536.
1125

1126 Nguyen, V.T., Song, C.H., Bae, B.U., Euh, D.J., 2013. Modeling of bubble coalescence and
1127 break-up considering turbulent suppression phenomena in bubbly two-phase flow.
1128 International Journal of Multiphase Flow 54, 31-42.
1129

1130 Ohkawa, K., Lahey Jr., R.T., 1980. The analysis of CCFL using drift-flux models. Nuclear
1131 Engineering and Design 61, 245-255.
1132

1133 Prince, M.J., Blanch, H.W., 1990. Bubble coalescence and break-up in air-sparged bubble
1134 columns. AIChE Journal 36, 1485-1499.
1135

1136 Rzehak, R., Krepper, E., 2013. CFD modeling of bubble-induced turbulence. International
1137 Journal of Multiphase Flow 55, 138-155.
1138

1139 Santarelli, C., Frohlich, J., 2015. Direct numerical simulations of spherical bubbles in vertical
1140 turbulent channel flow. International Journal of Multiphase Flow 75, 174-193.
1141

1142 Santarelli, C., Frohlich, J., 2016. Direct numerical simulations of spherical bubbles in vertical
1143 turbulent channel flow. Influence of bubble size and bidispersity. International Journal of
1144 Multiphase Flow 81, 27-45.
1145

1146 Serizawa, A., Kataoka, I., Michiyoshi, I., 1975. Turbulence structure of air-water flow bubbly
1147 flow-I. Measuring techniques. International Journal of Multiphase Flow 2, 221-233.
1148

1149 Speziale, C.G., Sarkar, S., Gatski, T.B., 1991. Modelling the pressure-strain correlation of
1150 turbulence: An invariant dynamical system approach. Journal of Fluid Mechanics 227, 245-
1151 272.
1152

1153 Sugrue, R., Magolan, B., Lubchenko, N., Baglietto, E., 2017. Assessment of a simplified set of
1154 momentum closure relations for low volume fraction regimes in STAR-CCM+ and
1155 OpenFOAM. *Annals of Nuclear Energy* 110, 79-87.
1156

1157 Sun, H., Kunugi, T., Shen, X., Wu, D., Nakamura, H., 2014. Upward air-water bubbly flow
1158 characteristics in a vertical square duct. *Journal of Nuclear Science and Technology* 51, 267-
1159 281.
1160

1161 Talley, J.D., Worosz, T., Kim, S., 2015. Characterization of horizontal air-water two-phase
1162 flow in a round pipe. Part II: Measurement of local two-phase parameters in bubbly flow.
1163 *International Journal of Multiphase Flow* 76, 223-236.
1164

1165 Tomiyama, A., Celata, G.P., Hosokawa, S., Yoshida, S., 2002a. Terminal velocity of single
1166 bubbles in surface tension dominant regime. *International Journal of Multiphase Flow* 28,
1167 1497-1519.
1168

1169 Tomiyama, A., Kataoka, I., Zun, I., Sakaguchi, T., 1998. Drag coefficients of single bubbles
1170 under normal and micro gravity conditions. *JSME International Journal Series B Fluids and
1171 Thermal Engineering* 41, 472-479.
1172

1173 Tomiyama, A., Tamai, H., Zun, I., Hosokawa, S., 2002b. Transverse migration of single
1174 bubbles in simple shear flows. *Chemical Engineering Science* 57, 1849-1858.
1175

1176 Troshko, A.A., Hassan, Y.A., 2001. A two-equation turbulence model of turbulent bubbly
1177 flows. *International Journal of Multiphase Flow* 27, 1965-2000.
1178

1179 Ullrich, M., Maduta, R., Jakirlic, S., 2014. Turbulent bubbly flow in a vertical pipe computed
1180 by an eddy-resolving Reynolds stress model, 10th International ERCOFTAC Symposium on
1181 Engineering Turbulence Modelling and Measurements (ETMM 10), Marbella, Spain,
1182 September 17-19.
1183

1184 Vasavada, S., Sun, X., Ishii, M., Duval, W., 2009. Benchmarking of the one-dimensional one-
1185 group interfacial area transport equation for reduced-gravity bubbly flows. *International
1186 Journal of Multiphase Flow* 35, 323-334.
1187

1188 Wang, S.K., Lee, S.J., Jones, O.C., Lahey, R.T., 1987. 3-D turbulence structure and phase
1189 distribution measurements in bubbly two-phase flows. *International Journal of Multiphase
1190 Flow* 13, 327-343.
1191

1192 Welleck, R.M., Agrawal, A.K., Skelland, A.H.P., 1966. Shape of liquid drops moving in liquid
1193 media. *AIChE Journal* 12, 854-862.
1194

1195 Woldesemayat, M.A., Ghajar, A.J., 2007. Comparison of void fraction correlations for
1196 different flow patterns in horizontal and upward inclined pipes. *International Journal of
1197 Multiphase Flow* 33, 347-370.
1198

1199 Yao, W., Morel, C., 2004. Volumetric interfacial area prediction in upward bubbly two-phase
1200 flow. *International Journal of Heat and Mass Transfer* 47, 307-328.
1201

1202 Yeoh, G.H., Tu, J.Y., 2006. Two-fluid and population balance models for subcooled boiling
1203 flow. *Applied Mathematical Modelling* 30, 1370-1391.